

Radiative contribution to the effective potential in composite Higgs models from lattice gauge theory

Thomas DeGrand,¹ Maarten Golterman,² William I. Jay,¹
Ethan T. Neil,^{1,3} Yigal Shamir,⁴ and Benjamin Svetitsky⁴

¹*Department of Physics, University of Colorado, Boulder, CO 80309, USA*

²*Department of Physics and Astronomy,*

San Francisco State University, San Francisco, CA 94132, USA

³*RIKEN-BNL Research Center, Brookhaven National Laboratory, Upton, NY 11973, USA*

⁴*Raymond and Beverly Sackler School of Physics and Astronomy,
Tel Aviv University, 69978 Tel Aviv, Israel*

Abstract

We develop methods to calculate the electroweak gauge boson contribution to the effective Higgs potential in the context of composite Higgs models, using lattice gauge theory. The calculation is analogous to that of the electromagnetic mass splitting of the pion multiplet in QCD. We discuss technical details of carrying out this calculation, including modeling of the momentum and fermion-mass dependence of the underlying current-current correlation function; direct integration of the correlation function over momentum; and fits based on the minimal-hadron approximation. We show results of a numerical study using valence overlap fermions, carried out in an SU(4) gauge theory with two flavors of Dirac fermions in the two-index antisymmetric representation.

I. INTRODUCTION

Composite Higgs theories [1, 2] have often been written down as effective field theories, typically non-linear sigma models [3–5]. In one approach, the sigma model describes a set of exactly massless Nambu–Goldstone bosons that live in a coset manifold G/H . This set contains the Higgs multiplet of the Standard Model (SM). The Higgs potential then comes mainly from coupling to the electroweak gauge bosons and to the top quark; this potential should induce the Higgs phenomenon of the SM. If the SM’s gauge symmetries are a subgroup of the unbroken symmetry H , then the coupling to the SM’s gauge bosons will induce a positive curvature at the origin of the Higgs potential, a phenomenon known as vacuum alignment [6]. A negative curvature, required in order to induce electroweak symmetry breaking, can then arise only from the top quark’s contribution.

The sigma model is only an effective low-energy description with the correct symmetry properties. A fuller understanding of the dynamics requires an underlying, ultraviolet-complete theory that gives rise to the non-linear sigma model at low energies. Several such proposals now exist in the literature [7–10], including an effort to catalogue ultraviolet completions [11, 12] that accommodate both a composite Higgs and a partially composite top quark [13].

Within such an ultraviolet completion, lattice simulations [14] can be used to determine low-energy constants of the theory, including the radiative contributions of the SM to the Higgs potential. In this paper, we present a lattice calculation for the gauge bosons’ part of the Higgs potential. This is given by¹ [3, 15, 16]

$$V_{\text{eff}} = C_{LR} \sum_Q \text{tr} (Q \Sigma Q^* \Sigma^*) , \quad (1.1)$$

where Σ is the non-linear field representing the multiplet of pseudo-Nambu–Goldstone bosons that contains the composite Higgs boson. The sum over Q runs over the $SU(2)_L$ generators gT_L^a and the hypercharge generator $g'Y$, with g and g' the corresponding coupling constants. In accordance with vacuum alignment, the low-energy constant C_{LR} is positive [16, 17], and the minimum of V_{eff} , given by $-C_{LR}(3g^2 + g'^2)$, is attained at $\langle \Sigma \rangle = \mathbf{1}$.

In principle, C_{LR} can be determined in a lattice calculation where the gauge bosons of both the new strong interaction and of the electroweak interactions are present as dynamical degrees of freedom. A more economical approach, which avoids the introduction of electroweak gauge bosons into the lattice simulation, is to obtain C_{LR} in terms of a correlation function of the ultraviolet theory,

$$C_{LR} = \int_0^\infty dq^2 q^2 \Pi_{LR}(q^2). \quad (1.2)$$

¹ This is the expression in the case of a coset of the form $SU(N)/SO(N)$, which is relevant to the model considered here. For other cosets the general form is similar. The top-sector contribution to the effective potential for the model of Ref. [8] was worked out in Ref. [15]. A lattice calculation of this contribution is more challenging.

Here $\Pi_{LR}(q^2)$ is the transverse part of the current–current correlation function,

$$\frac{1}{2}\delta_{ab}\Pi_{\mu\nu}(q) = -\int d^4x e^{iqx} \langle J_{\mu a}^L(x) J_{\nu b}^R(0) \rangle, \quad (1.3)$$

$$\Pi_{\mu\nu}(q) = (q^2\delta_{\mu\nu} - q_\mu q_\nu)\Pi_{LR}(q^2) + q_\mu q_\nu \Pi'(q^2). \quad (1.4)$$

The chiral currents are

$$\begin{aligned} J_{\mu a}^L &= \bar{\psi}\gamma_\mu(1 - \gamma_5)T_a\psi = V_{\mu a} - A_{\mu a}, \\ J_{\mu a}^R &= \bar{\psi}\gamma_\mu(1 + \gamma_5)T_a\psi = V_{\mu a} + A_{\mu a}, \end{aligned} \quad (1.5)$$

where T_a are the isospin generators. In the chiral limit, where the low-energy constant in Eq. (1.1) is defined, the current correlator (1.3) is automatically transverse.

Our task is related to a classic problem in hadronic physics. In quantum chromodynamics with two flavors, the pions are pseudo-Nambu–Goldstone bosons, massless in the chiral limit. The entire isotriplet gets most of its mass from chiral symmetry breaking by the quark masses; the charged pion gets an additional contribution from coupling to electromagnetism, lifting it above the neutral pion. Defining $\Delta m_\pi^2 \equiv m_{\pi^\pm}^2 - m_{\pi^0}^2$, we quote the sum rule derived long ago by Das et al. [18],

$$\Delta m_\pi^2 = -\frac{3\alpha}{4\pi f_\pi^2} \int_0^\infty dq^2 q^2 \Pi_{LR}(q^2)|_{m_q=0}. \quad (1.6)$$

This has served as the basis of lattice calculations of the pion mass difference that have been quite successful [19, 20].²

We present here a lattice calculation of the quantity C_{LR} in the context of composite Higgs theories. We study an SU(4) gauge theory with $N_f = 2$ Dirac fermions in the sextet representation of SU(4), which is the antisymmetric two-index representation—a real representation. We have studied this theory before [22], focusing on the phase diagram of the lattice theory and its particle spectrum. This theory is the first step towards a lattice simulation of the UV-complete composite Higgs model proposed in [8], in which 5 flavors of Majorana fermions in the sextet representation of SU(4) give rise to a composite Higgs within an SU(5)/SO(5) coset. The 5-Majorana theory can be studied on the lattice, but it requires the use of methods such as rational HMC (RHMC), which increase the computational cost compared to the theory with two Dirac fermions.³

As noted above, we require C_{LR} in the massless limit. In fact, $\Pi_{LR}(q^2)$ is an order parameter for the spontaneous breaking of chiral symmetry. Since we use Wilson–clover fermions in the action that generates gauge field configurations, chiral symmetry is not restored in the limit where the pion⁴ becomes massless (as long as the lattice spacing is nonzero). Thus we are led to use overlap fermions [23, 24], with exact chiral symmetry, to define correlation functions calculated on the gauge field ensembles. In this mixed-action

² For an early lattice discussion, see Ref. [21].

³ To construct SU(4) baryons that can couple linearly to the top quark, one must also add Dirac fermions in the fundamental (quartet) representation of SU(4). There are 3 flavors of them, making the baryons into an anti-triplet of ordinary color. The properties of this model have been studied at length in Refs. [8, 15].

We do not consider these in the present paper.

⁴ We use henceforth QCD terminology for the meson spectrum of our SU(4) gauge theory.

theory we can vary the valence (overlap) quark mass while keeping the dynamical (Wilson–clover) mass fixed, and approach a chiral limit in the former.⁵

$\Pi_{LR}(q^2)$ may be modeled by retaining only the pion and a_1 poles in the axial channel, and the ρ meson’s pole in the vector channel. This is the minimal-hadron approximation⁶ (MHA),

$$\Pi_{LR}(q^2) \approx \frac{f_\pi^2}{q^2} + \frac{f_{a_1}^2}{q^2 + m_{a_1}^2} - \frac{f_\rho^2}{q^2 + m_\rho^2}. \quad (1.7)$$

In the chiral limit, one can use the Weinberg sum rules [27] to eliminate f_ρ and f_{a_1} , giving

$$\Pi_{LR}(q^2) \approx \frac{f_\pi^2}{q^2} \frac{m_{a_1}^2 m_\rho^2}{(q^2 + m_{a_1}^2)(q^2 + m_\rho^2)}, \quad (1.8)$$

and thus

$$C_{LR} \approx f_\pi^2 \frac{m_{a_1}^2 m_\rho^2}{m_{a_1}^2 - m_\rho^2} \log \left(\frac{m_{a_1}^2}{m_\rho^2} \right). \quad (1.9)$$

In the QCD case, the MHA misses the experimental value of Δm_π^2 by 25%. Our numerical calculation of Π_{LR} enables us to test the approximation (1.7) directly in the present theory.

This paper deals more with technique than with results. Hence, while we present numerical data for two different lattice actions, we do not take either the continuum limit or the chiral limit for the dynamical (“sea”) fermions. Indeed, the two ensembles that we study produce values of C_{LR} that are in disagreement. As we have stated above, the theory studied here is not quite an actual model for a composite Higgs boson. This is why we stop short of an extrapolation to the continuum limit, which would involve considerable additional computation for a theory that is, after all, not of direct physical interest.

Our paper is organized as follows. In Sec. II we present the technical aspects of our lattice simulations. We specify the lattice action with which we generated configurations, and we describe the measurement of $\Pi_{LR}(q^2)$, defined via overlap valence fermions, on these configurations. We then proceed to our numerical work. We generated two ensembles with different lattice actions; we present the ensembles and their particle spectra in Sec. III. Once $\Pi_{LR}(q^2)$ is in hand, the integration in Eq. (1.2) is straightforward, except for handling the pole in Π_{LR} at $q = 0$. We show one way to do this in Sec. IV. In Sec. V, we demonstrate an alternative method for calculation of C_{LR} , fitting $\Pi_{LR}(q^2)$ to a rational function inspired by the MHA. We find that the two methods for extracting C_{LR} produce results that agree well, for each ensemble. Our conclusions are in Sec. VI.

We give some details about the lattice action in Appendix A and review some current algebra in Appendix B. In Appendix C we describe an attempt to reconcile our two ensembles using chiral perturbation theory.

⁵ Previous calculations of $\Pi_{LR}(q)$ in QCD and beyond [19, 25, 26], have also used overlap (or domain-wall) fermions.

⁶ We note that the location of the pole at $q^2 = 0$ does not depend on the chiral limit; see Appendix B.

II. LATTICE ACTION AND OVERLAP VALENCE FERMIONS

A. Wilson–clover action with dislocation suppression

We generate ensembles of gauge configurations with the lattice action,

$$S = S_{\text{plaq}} + S_f + S_{\text{NDS}}. \quad (2.1)$$

Here S_{plaq} is the usual plaquette action for the fundamental gauge fields $U_{x\mu}$. The fermion action S_f is comprised of the conventional Wilson hopping term and a clover term [28], where the gauge connection in both terms is constructed from $U_{x\mu}$ in two steps: normalized hypercubic (nHYP) smearing [29–31] followed by promotion to the sextet representation. Finally the term S_{NDS} is a pure gauge term designed to suppress dislocations in the dynamical gauge field, in order to help eliminate spikes in the fermion force and to ease the calculation of the overlap operator (see Appendix A and Ref. [32]).

The action is identical to that used in our earlier study [22], except for the introduction of the NDS term. The gauge coupling is set by the coefficients β and γ of the plaquette and NDS terms: at tree level,

$$\frac{1}{g_0^2} = \frac{\beta}{2N_c} + \frac{\gamma}{N_c} \left(\frac{\alpha_1}{3} + \alpha_2 + \alpha_3 \right), \quad (2.2)$$

where α_i are the smearing parameters and we have adopted a common γ for the three levels of smearing. Our smearing parameters took the values $(\alpha_1, \alpha_2, \alpha_3) = (0.75, 0.6, 0.3)$.

The theory contains two degenerate flavors of sea quarks, whose common bare mass is introduced via the hopping parameter $\kappa = (2m_0a + 8)^{-1}$. As is appropriate for nHYP smearing [33], the clover coefficient is set to its tree level value, $c_{\text{SW}} = 1$. Since the sextet is a real representation of the gauge group, the global symmetry of the continuum theory is $\text{SU}(4)$, which breaks spontaneously to $\text{SO}(4)$; in the lattice theory, on the other hand, the Wilson term breaks the $\text{SU}(4)$ explicitly to $\text{SO}(4)$. As noted in Ref. [22], the nHYP smearing procedure introduces a small violation of the reality of the sextet gauge links. This is a lattice artifact which breaks the degeneracies expected by virtue of the $\text{SO}(4)$ symmetry. We leave this uncorrected in the generation of gauge configurations, but we do apply a correction when we use the gauge configurations to calculate fermionic observables. Thus the correlation functions of fermionic operators indeed satisfy the $\text{SO}(4)$ symmetry. Like other differences between sea quarks and valence quarks, the effects of this correction will disappear with the lattice spacing.

B. Overlap operator

For the valence quarks and their currents, we use an overlap operator. Our implementation is as described in Refs. [34–38]. The massless overlap operator is defined as

$$D(0) = R_0 \left(1 + \frac{d(-R_0)}{\sqrt{d^\dagger(-R_0)d(-R_0)}} \right). \quad (2.3)$$

Here $d(m) = d + m$, where d is a massless Wilson–Dirac operator on the lattice. We choose one with nearest- and next-nearest-neighbor interactions, plus a clover term; we set $R_0 = 1.2$.

Adding a valence fermion mass m_v gives the operator

$$D(m_v) = \left(1 - \frac{m_v}{2R_0}\right) D(0) + m_v. \quad (2.4)$$

We evaluate the correlation function in Π_{LR} using improved currents. The vector current is

$$V_{\mu a} = \bar{q}\gamma_\mu T_a \left(1 - \frac{aD(0)}{2R_0}\right) q, \quad (2.5)$$

while the axial current is

$$A_{\mu a} = \bar{q}\gamma_\mu\gamma_5 T_a \left(1 - \frac{aD(0)}{2R_0}\right) q. \quad (2.6)$$

These currents are not conserved, and so the correlator of each current has a quadratically divergent contact term. Thanks to a chiral Ward identity, the quadratic divergence cancels in the vector–axial difference.

In the actual computation of the correlator, we move the overlap operator out of the currents and into the quark propagator. We replace the currents (2.5)–(2.6) by point currents and the quark propagator D^{-1} by the “shifted” propagator [39, 40]

$$\hat{D}^{-1}(m_v) = \frac{1}{1 - m_v/(2R_0)} \left[D^{-1}(m_v) - \frac{1}{2R_0} \right]. \quad (2.7)$$

We compute eigenvalues of the squared Hermitian Dirac operator $D^\dagger D$ with the `Primme` package [41]; these are used to precondition the calculation of propagators.

C. Extraction of Π_{LR}

As noted in the introduction, $\Pi_{LR}(q^2)$ is an order parameter for chiral symmetry. Thanks to our use of overlap fermions, this remains true on the lattice, with the currents defined in the preceding subsection. In analogy with Eq. (1.3), we define the lattice vacuum polarization via

$$\frac{1}{2}\delta_{ab}\Pi_{\mu\nu}^{\text{lat}}(q) = - \sum_x e^{iqx} \langle J_{\mu a}^L(x) J_{\nu b}^R(0) \rangle. \quad (2.8)$$

We would like to decompose this as in Eq. (1.4). Lattice artifacts, however, make the structure of $\Pi_{\mu\nu}^{\text{lat}}(q)$ more complex,

$$\Pi_{\mu\nu}^{\text{lat}}(q) = P_{\mu\nu}^T(q)\Pi_{LR}(q) + P_{\mu\nu}^L(q)\Pi'(q) + \dots \quad (2.9)$$

where $P^T(q)$ and $P^L(q)$ are lattice analogs of the transverse and longitudinal projectors (see below). The dots represent additional terms that are proportional to higher powers of q_μ (and of the lattice spacing) and that break rotational invariance [42].

We deal with these lattice artifacts empirically, following the method of Refs. [19, 43]. For each lattice momentum q , we do a fit to $\Pi_{\mu\nu}^{\text{lat}}(q)$, treating Π_{LR} and Π' as fit parameters. This means that we form the χ^2 function for each individual momentum mode q ,

$$\chi_q^2 = \sum_{\mu\nu} \left[\Pi_{\mu\nu}^{\text{lat}}(q) - P_{\mu\nu}^T(q)\Pi_{LR}(q) - P_{\mu\nu}^L(q)\Pi'(q) \right]^2, \quad (2.10)$$

taking the sixteen $\Pi_{\mu\nu}^{\text{lat}}$ correlators as the quantities to be fit. Here

$$\begin{aligned} P_{\mu\nu}^T(q) &= \hat{q}^2 \delta_{\mu\nu} - \hat{q}_\mu \hat{q}_\nu, \\ P_{\mu\nu}^L(q) &= \hat{q}_\mu \hat{q}_\nu \end{aligned} \quad (2.11)$$

are the transverse and longitudinal lattice projectors. In a slight variation on the method of Ref. [19], we use $\hat{q}_\mu = (2/a) \sin(q_\mu a/2)$ in Eq. (2.11). As usual, $q_\mu = (2\pi/L_\mu)n_\mu$ for periodic boundary conditions with period L_μ .

The minimization of χ_q^2 with respect to Π_{LR} and Π' reduces to the simple weighted averages,

$$\Pi_{LR}(q) = \frac{\sum_{\mu\nu} P_{\mu\nu}^T(q) \Pi_{\mu\nu}^{\text{lat}}(q)}{3(\hat{q}^2)^2}, \quad (2.12)$$

$$\Pi'(q) = \frac{\sum_{\mu\nu} P_{\mu\nu}^L(q) \Pi_{\mu\nu}^{\text{lat}}(q)}{(\hat{q}^2)^2}. \quad (2.13)$$

The success of the decomposition is quantified by calculating

$$\Delta(q) = \sum_{\mu\nu} \hat{q}_\mu \hat{q}_\nu \left(\frac{1}{\hat{q}^2} - \frac{\hat{q}_\nu}{\sum_\lambda \hat{q}_\lambda^3} \right) \Pi_{\mu\nu}^{\text{lat}}(q). \quad (2.14)$$

If $\Pi_{\mu\nu}^{\text{lat}}$ is truly a superposition of pure longitudinal and transverse terms [with lattice projectors (2.11)], then $\Delta = 0$. We find that the projection works well in our numerical results, observing that $\Delta \ll \Pi_{LR}(q)$ up to $q^2 \sim 20$. For q^μ oriented along the axes of the lattice, the projection is satisfied exactly, that is, $\Delta = 0$ as expected.

Because of the transverse projector, $\Pi_{LR}(q)$ is not defined at $q = 0$. For a finite volume, however, when momenta are discrete, the momentum region around $q = 0$ can give a significant contribution to the integral (1.2). We handle this region by extrapolation from finite q , as will be seen below.

III. ENSEMBLES AND SPECTRA

One aim of our study was to compare results for different lattice approximations, and so we created ensembles of configurations for two different values of the NDS coefficient γ , with values of (β, κ) chosen to give approximately equal physical scales. We chose the gauge couplings $(\beta, \gamma) = (7.8, 0.125)$ and $(6.0, 0.25)$ and a lattice size of $12^3 \times 24$ sites. For each coupling we performed a scan of sea quark κ values. We measured the usual unquenched (i.e., Wilson–clover) spectroscopic quantities—meson masses and decay constants—as well as the Sommer parameter r_1 from the static potential. We then selected one value of κ for each gauge coupling to use in the calculation of $\Pi_{\mu\nu}(q)$.

We list the two ensembles in Table I and the measured observables in Table II. As in our earlier work [22], the quark mass m_q given in Table II is defined through the axial Ward identity, which relates the divergence of the axial current $A_\mu^a = \bar{\psi} \gamma_\mu \gamma_5 (\tau^a/2) \psi$ to the pseudoscalar density $P^a = \bar{\psi} \gamma_5 (\tau^a/2) \psi$. At zero three-momentum we have

$$\partial_t \sum_{\mathbf{x}} \langle A_0^a(\mathbf{x}, t) \mathcal{O}^a \rangle = 2m_q \sum_{\mathbf{x}} \langle P^a(\mathbf{x}, t) \mathcal{O}^a \rangle, \quad t > 0, \quad (3.1)$$

	Ensemble 1	Ensemble 2
β	6.0	7.8
γ	1/4	1/8
κ	0.128	0.130
κ_c	0.1312	0.1314
Volume	$12^3 \times 24$	$12^3 \times 24$
Configurations	600	400

TABLE I: Parameters of the two ensembles we analyzed: gauge coupling β , NDS coupling γ , hopping parameter κ (and κ_c for comparison), lattice volume, and the number of saved configurations. In both ensembles, configurations were separated by four trajectories of unit length. In the runs of ensemble 1 the acceptance was 90%, while in those of ensemble 2 it was 80%. We determined κ_c by linear extrapolation of m_q (see Table II) to zero.

	Ensemble 1	Ensemble 2
m_q	0.102(1)	0.048(1)
m_π	0.575(2)	0.392(3)
m_ρ	0.750(3)	0.617(8)
m_{a_1}	1.018(5)	0.831(13)
f_π	0.190(1)	0.140(3)
r_1	3.09(5)	3.08(6)

TABLE II: Measured observables for the two ensembles described in Table I: Quark mass m_q from the axial Ward identity, meson masses m_i , decay constant f_π , and Sommer parameter r_1 . The spectra and f_π are constructed from the same Wilson–clover fermions used in generating the ensembles.

where \mathcal{O}^a is a source at $t = 0$, here taken to be a smeared “Gaussian shell.” The critical value κ_c is determined through the vanishing of the quark mass m_q . The decay constant f_π has the continuum definition

$$\langle 0 | A_\mu^a(x) | \pi^b(p) \rangle = i p_\mu f_\pi \delta^{ab} e^{ipx}. \quad (3.2)$$

In the lattice calculation it is extracted from the “raw” value f_π^{raw} via [44]

$$f_\pi = (1 - 0.75\kappa/\kappa_c) f_\pi^{\text{raw}}. \quad (3.3)$$

The values of r_1 are the same in the two ensembles, indicating that the physical lattice size is the same; also the value of r_1 shows that the spatial volumes are large enough that confinement physics is undisturbed. Ensemble 2 is somewhat closer to the massless limit than ensemble 1. The chosen values of κ represent the lightest sea quark masses for which the hadronic observables do not show strong effects of finite volume. Since we take the chiral limit, below, by varying valence masses, we do not venture towards lighter sea quarks. We omit further discussion of the selection of κ values—the analysis is fairly standard and this is not the focus of our work.

m_v	m_π	m_ρ	m_{a_1}	f_π
0.100	0.560(2)	0.745(4)	1.027(7)	0.175(1)
0.075	0.479(2)	0.690(5)	0.975(7)	0.162(1)
0.050	0.388(3)	0.636(7)	0.921(9)	0.149(1)
0.035	0.325(4)	0.608(10)	0.886(10)	0.140(2)
0.025	0.284(3)	0.617(11)	0.879(15)	0.135(2)
0.020	0.257(3)	0.621(9)	0.846(13)	0.128(2)
0.015	0.227(5)	0.629(33)	0.853(18)	0.127(2)
0.010	0.195(6)	0.617(12)	0.818(16)	0.120(3)

TABLE III: Valence overlap spectra for ensemble 1. m_v is the valence quark mass. Note that the order of the lines, here and below, is from heavy to light valence quarks, towards the chiral limit. We do not show results for m_q , extracted from Eq. (3.1), because it is equal to m_v to the precision shown.

We then computed $\Pi_{\mu\nu}(q)$ using valence overlap fermions on the two ensembles, for eight values of the valence quark mass ranging from $m_v = 0.01$ to 0.10. We also supplemented the Wilson–clover observables of Table II with overlap spectra for these masses. The spectral calculations were separate from the calculations of $\Pi_{\mu\nu}(q)$ since the inversions used a Coulomb-gauge Gaussian source rather than a point source. These mixed-action data are collected in Tables III and IV.

We vary the valence quark mass into a regime much lighter than the sea quark, and hence it gives us a handle for checking for chiral logarithms and finite-volume effects. A plot of m_π^2/m_v (see Fig. 1) shows a common plateau in this ratio for $m_v \gtrsim 0.05$ for the two ensembles, which have a common scale r_1 . We note that in each ensemble the sea pion lies comfortably in the plateau furnished by the valence pion.

We can account for the deviations from this plateau using next-to-leading-order (NLO) mixed-action chiral perturbation theory (χ PT). The steps needed to obtain the NLO correction for the mass of the valence pion are similar to those discussed in Appendix C for the case of the valence pion’s decay constant. A fit to the data in Fig. 1 with free parameters gives a valid description of the data.

The p -regime NLO χ PT formula is comprised of an infinite-volume chiral logarithm and a finite-volume correction. Because the parameters of the fit are poorly determined, we do not know the relative size of these pieces, nor indeed can we tell whether we are in fact in the p -regime. If we rewrite the χ PT formulas in terms of the valence pion’s mass and decay constant, and then estimate them using the spectroscopic data, the result suggests that an appreciable part of the increase in the pion mass seen in Fig. 1 at small m_v originates in finite-volume effects. Future studies will require larger volumes to accommodate light sea pions as well as to reduce the squeezing of the valence pions.

m_v	m_π	m_ρ	m_{a_1}	f_π
0.100	0.569(2)	0.763(3)	0.957(9)	0.173(1)
0.075	0.487(3)	0.701(5)	0.888(0)	0.159(1)
0.050	0.396(4)	0.651(6)	0.817(3)	0.142(1)
0.035	0.343(3)	0.620(9)	0.775(6)	0.130(1)
0.025	0.290(4)	0.615(12)	0.790(16)	0.120(2)
0.020	0.270(4)	0.613(11)	0.734(23)	0.113(2)
0.015	0.233(5)	0.601(18)	0.764(20)	0.107(2)
0.010	0.206(7)	0.600(17)	0.678(35)	0.099(3)

TABLE IV: Valence overlap spectra for ensemble 2.

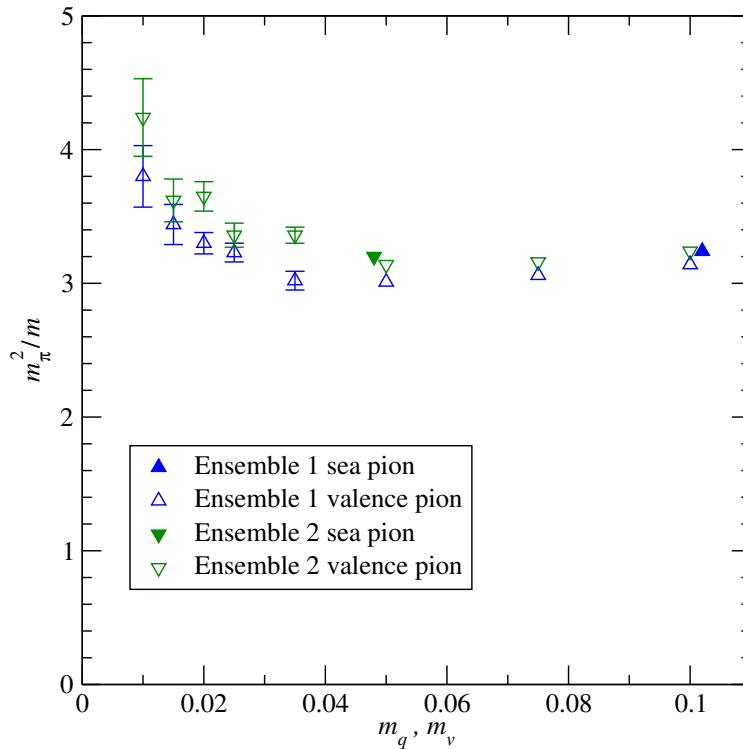


FIG. 1: PCAC ratio m_π^2/m for valence and sea pions in the two ensembles. For the valence pions, $m \equiv m_v$, the valence quark mass, while for the sea pions $m \equiv m_q$, the quark mass measured from the axial Ward identity. Error bars are suppressed if smaller than the plotted symbols.

IV. C_{LR} VIA DIRECT INTEGRATION

A. Ultraviolet cutoff

As a preliminary step, let us determine the expected dependence of C_{LR} on an ultraviolet cutoff M . In infinite volume, the value of C_{LR} depends on the dynamical infrared scale Λ of the theory,⁷ on the fermion mass m , and on M . We consider the operator product expansion for the two-current correlator, which is, schematically,

$$\Pi_{XX}(q^2; m) \sim 1 + \frac{m^2}{q^2} + \frac{g^2 \langle G_{\mu\nu} G_{\mu\nu} \rangle + m \langle \bar{\psi}\psi \rangle}{q^4} + \frac{\Lambda^6}{q^6} + \dots, \quad (4.1)$$

where $XX = VV$ or AA . Each term is to be multiplied by a coefficient function that depends logarithmically on q^2 . Note that the first two terms have a perturbative origin. The $1/q^6$ term comes from several dimension-6 operators. In the difference $VV - AA$, the identity term drops out, as do all purely gluonic condensates, and we have

$$\Pi_{LR}(q^2; m) \sim \frac{m^2}{q^2} + \frac{m\Lambda^3}{q^4} + \frac{\Lambda^6}{q^6} + \dots, \quad (4.2)$$

where, for each power of $1/q^2$, we show only the leading dependence on the fermion mass: in particular, $\langle \bar{\psi}\psi \rangle \sim \Lambda^3 + \mathcal{O}(m)$.

Introducing the ultraviolet cutoff via

$$C_{LR}(m; M) = \int_0^{M^2} dq^2 q^2 \Pi_{LR}(q^2; m), \quad (4.3)$$

we have

$$\frac{\partial C_{LR}}{\partial M^2} = M^2 \Pi_{LR}(M^2; m). \quad (4.4)$$

Upon using Eq. (4.2) and integrating Eq. (4.4), we find after taking the chiral limit that

$$C_{LR}(0; M) = \lim_{m \rightarrow 0} C_{LR}(m; M) \sim \Lambda^4 + \frac{\Lambda^6}{M^2}, \quad (4.5)$$

where Λ^4 is the integration constant. This shows that the dependence of $C_{LR} = \lim_{M \rightarrow \infty} C_{LR}(0; M)$ on the ultraviolet cutoff vanishes. This result could have been anticipated by noting that C_{LR} is an order parameter for the spontaneous breaking of chiral symmetry.

In our numerical calculation we use a discretized version of Eq. (4.3). Since we use chiral valence fermions, the above conclusion applies also on the lattice. We impose an upper limit M in the summation over momenta, along the lines of Eq. (4.3), with $M < \pi/a$. For non-zero (valence) mass, one expects the dependence of $C_{LR}(m; M)$ on M to follow from Eqs. (4.2) and (4.4) and hence to contain a quadratically divergent term $\sim m^2 M^2$. In practice, we have seen very little variation of C_{LR} with M once M is sufficiently large. We offer an explanation of this state of affairs in Sec. V D below.

⁷ Here we are concerned with the dependence of C_{LR} on the ultraviolet cutoff, for which it suffices to have a rough idea of the dynamical infrared scale. For a detailed discussion, see Sec. IV C below.

B. Summing $\Pi_{LR}(q)$ over the lattice momentum

The calculation of current–current correlators described above gives us $\Pi_{LR}(q_\mu)$ at all 4-momenta (except for $q_\mu = 0$) for a finite lattice, at a given valence mass m_v , where we now consider Π_{LR} as a function of q_μ , rather than q^2 . We write Eq. (1.2) in infinite volume as

$$C_{LR} = 16\pi^2 \int \frac{d^4q}{(2\pi)^4} \Pi_{LR}(q_\mu), \quad (4.6)$$

and integrate directly in four dimensions. Having in mind a space-time lattice of dimensions $V = L_s^3 \times L_t$, we define the cells in q space such that the side μ of a cell has length $2\pi/L_\mu$. We break the integral (4.6) into a sum of cell integrals,

$$C_{LR} = \frac{16\pi^2}{V} \sum_{q_\mu} \Pi_{LR}^d(q_\mu). \quad (4.7)$$

In Eq. (4.7), $\Pi_{LR}^d(q_\mu)$ is a discrete quantity, the average of the continuum quantity over the cell in momentum space centered on q_μ :

$$\Pi_{LR}^d(q_\mu) = \prod_\nu \left[\frac{L_\nu}{2\pi} \int_{q_\nu - \pi/L_\nu}^{q_\nu + \pi/L_\nu} dq'_\nu \right] \Pi_{LR}(q'_\mu). \quad (4.8)$$

Where Π_{LR} is smooth, Eq. (4.8) can be approximated by replacing $\Pi_{LR}^d(q'_\mu) \rightarrow \Pi_{LR}(q_\mu)$. That is, we proceed just to sum in Eq. (4.7) the values of Π_{LR} at the centers of the cells, which are the given lattice data.

The exception is the cell centered on $q_\mu = 0$, where Eq. (1.7) tells us that Π_{LR} has a pole. We approximate the integrand in Eq. (4.8) by its pole plus a constant pedestal,

$$\Pi_{LR}(q_\mu) \simeq p + \frac{f_\pi^2}{q^2}, \quad (4.9)$$

where we take the value of f_π from the spectroscopic data, Tables III and IV. For this cell, then,

$$\Pi_{LR}^d(0) \simeq p + \frac{A f_\pi^2}{16\pi^2} L_s^2, \quad (4.10)$$

where

$$A = \int_{-1}^1 d^4x \frac{1}{\mathbf{x}^2 + (x_0/b)^2}, \quad (4.11)$$

and we define $b = L_t/L_s$. The integral for A is readily evaluated for our lattice shape,

$$A(b=2) \doteq 22.5095963 \dots . \quad (4.12)$$

Inserting into Eq. (4.10) and thence into Eq. (4.7), the contribution of the pole to C_{LR} comes to

$$\frac{L_s^2}{V} \times A f_\pi^2. \quad (4.13)$$

While other cells' contributions to C_{LR} go as $1/V$, the pole at $q = 0$ gives a term $\propto L_s^2/V$, which grows in relative importance as L_s grows.

The contribution of the pedestal to C_{LR} is $(16\pi^2/V)p$. The pedestal p can be estimated from the average over some set of cells surrounding the $q = 0$ cell. Collecting m cells at momenta $\{q_\mu^a, a = 1, \dots, m\}$, we approximate from Eq. (4.9)

$$\sum_a \Pi_{LR}^d(q^a) = mp + f_\pi^2 \sum_a \frac{1}{(q^a)^2}, \quad (4.14)$$

and thus

$$p = \frac{1}{m} \sum_{a=1}^m \left(\Pi_{LR}^d(q^a) - f_\pi^2 \frac{1}{(q^a)^2} \right). \quad (4.15)$$

That is, p is the average of the discrete Π_{LR}^d in the neighboring cells, minus the pole term on those cells.

For this analysis, we made use of six of the eight valence masses, not including the $m_v = 0.015$ and 0.025 data, which were added only later for use with the fitting method discussed in the next section. The extrapolations to $m_v = 0$ are well constrained without the additional valence masses. Our results are listed in Table V and plotted in Fig. 2.

The contribution to C_{LR} of the cell at $q = 0$ ranges from about 8% of the total for the largest m_v to 20% for the smallest, in both ensembles. The error bars stand in the same proportion, so the error in Eq. (4.10) is not significant in the overall error in C_{LR} . This of course may change when the lattice dimensions are changed.

In reaching the results shown in Table V, we included in the pedestal (4.15) only the nearest neighbors of $q = 0$, namely, the cells displaced by ± 1 on the time axis, which are at $q_4 = \pm 2\pi/24$. To vary this procedure we included next-nearest neighbors as well. This means adding the nearest neighbors in the $\pm x$, $\pm y$, and $\pm z$ directions, as well as the next-nearest neighbors in the time direction (all of these have $|q| = 2\pi/12$). Comparing the two pedestal recipes shows a shift of a few percent in $C_{LR}(m_v)$ at small masses, causing an upward shift of 4% and 7% in the chiral extrapolations of Ensemble 1 and Ensemble 2, respectively. In all cases these are smaller than the statistical error, so we cannot estimate the systematic error due to this part of the algorithm.

C. Chiral extrapolation

C_{LR} is a quantity that involves an integral over all momenta. Moreover, in QCD, it is experimentally known that the spectral functions are dominated by momenta on the order of the ρ and a_1 masses. It is therefore not straightforward to use ChPT to perform the extrapolation in m_v to $m_v = 0$. At a practical level, while chiral logarithms may be present (originating from the low- q^2 part of the integral), we find that we are not sensitive to these within our statistics. Thus, instead, we adopt a simple power-law fit,

$$C_{LR}(m_v) = c_0 + c_1 m_v + c_2 m_v^2 + c_3 m_v^3 + \dots, \quad (4.16)$$

giving c_0 as the chiral limit. In practice, we see no advantage to going beyond a cubic. The result is indicated in Table V and in Fig. 2.

Strictly speaking, the form of Eq. (4.16) is not adequate for a calculation involving chiral valence propagators evaluated on a Wilson–clover sea. Zero modes in the valence sector are not suppressed by the Wilson–clover determinant, and hence correlation functions such as

m_v	$C_{LR}(m_v)$	
	Ensemble 1	Ensemble 2
0.100	0.02998(31)	0.03100(61)
0.075	0.02145(25)	0.02179(55)
0.050	0.01391(20)	0.01350(47)
0.035	0.00998(17)	0.00913(41)
0.020	0.00658(17)	0.00534(33)
0.010	0.00460(17)	0.00325(26)
extrapolated $C_{LR}(0)$	0.00293(15)	0.00151(18)
restricted fit		0.00140(19)

TABLE V: C_{LR} calculated for the two ensembles, at six values of the valence mass m_v , followed by the extrapolation to $m_v = 0$ via a cubic [cf. Eq. (4.16), and see Fig. 2]. The fit of Ensemble 1 gives $\chi^2/\text{d.o.f.} = 1.0/2$. For Ensemble 2, the cubic fit to all the data points gave $\chi^2/\text{d.o.f.} = 7.4/2$. The last line is the result of a fit that drops the highest-mass point, $m_v = 0.100$, giving a satisfactory $\chi^2/\text{d.o.f.} = 1.2/1$.

Π_{LR} will contain inverse powers of m_v .⁸ Because all exact zero modes in any configuration have the same chirality, the structure of Π_{LR} [Eq. (1.3)] implies that only one propagator at a time can be saturated by a valence zero mode. This should lead to a $1/(m_v\sqrt{V})$ divergence at small m_v , where the dependence on the volume V reflects the density of exact zero modes. We observe that all our valence chiral extrapolations have good χ^2 without an added $1/m_v$ term. We conclude that this effect will show up only at smaller valence masses than the ones used in this study and/or with improved statistics.

The values of C_{LR} in the chiral limit for the two ensembles differ by a factor of 2, which amounts to more than 6σ , as measured by the statistical errors. Presumably the origin of this discrepancy is in the difference in lattice actions. Of all the hadronic observables measurable on the ensembles, the value of f_π has entered directly into our determination of C_{LR} , and indeed the MHA, Eq. (1.9), gives a direct proportionality between C_{LR} and f_π^2 . We see in Tables III and IV that $f_\pi(m_v)$ of the valence quarks in the two ensembles agrees for large quark masses but diverges for light masses. We therefore attempt to reconcile the ensembles in their chiral limits by rescaling C_{LR} by a factor of f_π^2 . Figure 3 shows the rescaled quantity C_{LR}/f_π^2 for each ensemble.

Equation (1.9) indicates that the ratio C_{LR}/f_π^2 is given by some scale Λ^2 that stems from the non-Nambu–Goldstone spectrum, that is, from the infrared physics associated with confinement. As a stand-in for this scale we can take $1/r_1$, since r_1 characterizes the confinement distance of the heavy-quark potential. Referring to Table II and Fig. 3, the extrapolations to $m_v = 0$ give the dimensionless ratios

$$\frac{r_1^2 C_{LR}}{f_\pi^2} = \begin{cases} 2.37(24) & \text{Ensemble 1} \\ 2.21(28) & \text{Ensemble 2} \end{cases} \quad (4.17)$$

so that perhaps the discrepancy in f_π captures the departure of our ensembles from the

⁸ This effect was studied in the quenched approximation in Ref. [45]. For a discussion in the context of mixed action, see for example Refs. [46, 47].

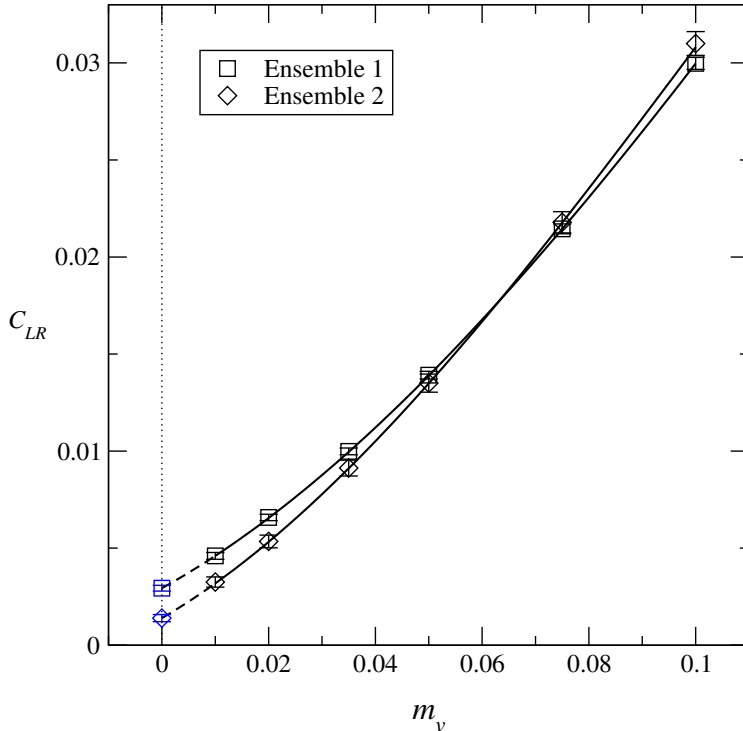


FIG. 2: $C_{LR}(m_v)$ for the two ensembles as listed in Table V. The extrapolations to $m_v = 0$ are cubic fits. The fit for Ensemble 2 drops the point at $m_v = 0.1$.

continuum limit as $m_v \rightarrow 0$ (we recall that r_1 is the same in the two ensembles). If this is the case, then the path to reconciling the two ensembles might be found in fitting the dependence of the valence f_π on the valence mass m_v , for both ensembles together, through chiral perturbation theory. An attempt to do this is detailed in Appendix C.

Theories with fermions in two-index representations have been studied in a $1/N_c$ framework [48], as an alternative to the original $1/N_c$ expansion that deals with fermions in the fundamental representations. Either expansion can in principle be applied to QCD, because for $N_c = 3$ the fundamental and two-index anti-symmetric representations are the same. It is therefore interesting to compare the value of the ratio (4.17) with the QCD value. Using Eqs. (1.2) and (1.6), $m_\pi^+ - m_\pi^0 = 4.6$ MeV, and $r_1 = 0.32$ fm, we have in QCD

$$\frac{r_1^2 C_{LR}}{f_\pi^2} = 1.9 \quad (\text{QCD}) . \quad (4.18)$$

The comparison to Eq. (4.17) may bespeak the validity of large- N arguments.

V. C_{LR} VIA FITTING $\Pi_{LR}(q^2)$

A. Modeling $\Pi_{LR}(q^2)$ and the MHA

An alternative approach to evaluation of the integral (1.2) is to fit the integrand $q^2 \Pi_{LR}(q^2)$ to a smooth function of q^2 . If the fit function is extended down to $q^2 = 0$ then its integral

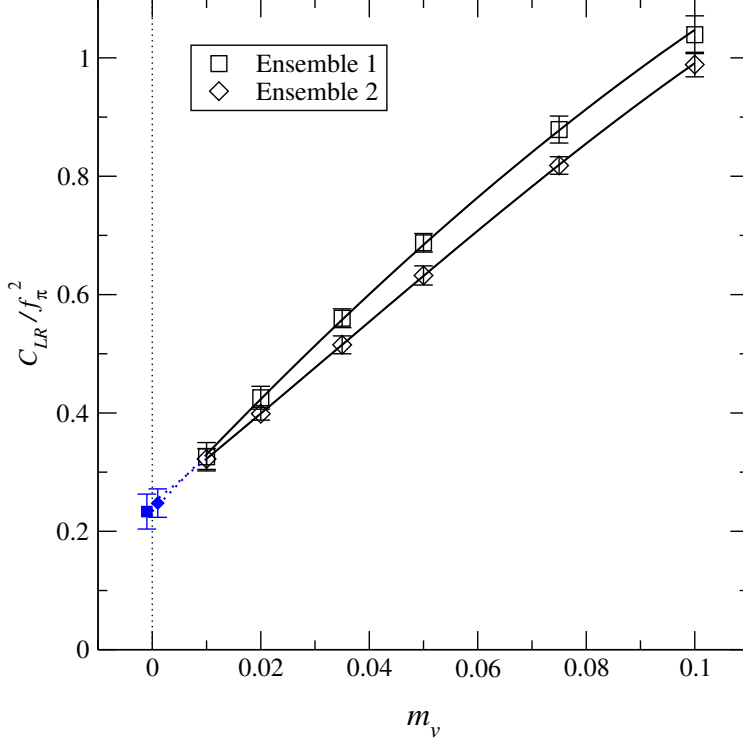


FIG. 3: $C_{LR}(m_v)$ rescaled by $f_\pi^2(m_v)$. The extrapolations to $m_v = 0$ are cubic fits; the extrapolated points are displaced horizontally for clarity.

will automatically incorporate the contribution to C_{LR} from the $q^2 \simeq 0$ region. We find that a model function inspired by the MHA, Eq. (1.7), describes our data well when m_v is small enough. Our fits thus provide a useful cross-check of our direct integration result for C_{LR} , and at the same time testify to the applicability of the MHA.

Equation (1.7) has two poles at $q^2 < 0$ and one at $q^2 = 0$, so that the function $q^2\Pi_{LR}(q^2)$ in this approximation is finite as $q^2 \rightarrow 0$ and smooth at positive q^2 . We can rewrite it as a rational function of q^2 with five parameters,

$$x\Pi_{LR}(x) = a_0 \left(\frac{a_1x + 1}{a_2x^2 + a_3x + 1} \right) + b, \quad (5.1)$$

where $x \equiv q^2$. By comparing Eq. (5.1) to Eq. (1.7), we can identify the values of the parameters predicted by the MHA:

$$\begin{aligned} a_0 &= f_\rho^2 - f_{a_1}^2, \\ a_1 &= \frac{f_\rho^2 m_\rho^2 - f_{a_1}^2 m_{a_1}^2}{m_\rho^2 m_{a_1}^2 (f_\rho^2 - f_{a_1}^2)}, \\ a_2 &= \frac{1}{m_\rho^2 m_{a_1}^2}, \\ a_3 &= \frac{1}{m_\rho^2} + \frac{1}{m_{a_1}^2}, \\ b &= f_{a_1}^2 + f_\pi^2 - f_\rho^2. \end{aligned} \quad (5.2)$$

As a test of the MHA, we use these relations and our fit results to derive the masses and decay constants from $\Pi_{LR}(q^2)$. These may then be compared to results for the same quantities from spectroscopy. We note, however, that there is no a priori reason that the fit parameters of the rational function have to agree with the spectroscopic quantities. The 3-pole form may be a poor approximation to the multiparticle cuts that characterize the physical current correlation function [49].

The Weinberg sum rules [27] follow in the chiral limit from the requirement that $\Pi_{LR} \sim q^{-6}$ as $q^2 \rightarrow \infty$ [cf. Eq. (4.2)]. Combined with the MHA, the sum rules imply the relations

$$f_\pi^2 = f_\rho^2 - f_{a_1}^2 \quad (5.3)$$

and

$$f_{a_1}^2 m_{a_1}^2 = f_\rho^2 m_\rho^2. \quad (5.4)$$

In terms of our MHA-inspired fit function (5.1), the first condition implies that $a_0 = f_\pi^2$ and $b = 0$, while the second condition gives $a_1 = 0$. At finite mass, we find that our fits to $q^2 \Pi_{LR}(q^2)$ require us to keep all five parameters non-zero, but the coefficients a_1 and b do appear to be consistent with zero in the chiral limit (see Sec. V C below).

B. Fitting details

For each ensemble and at each value of the valence fermion mass m_v , we carry out fully correlated, unconstrained least-squares fits to the data for $q^2 \Pi_{LR}(q^2)$, making use of the standard `lsqfit` non-linear fitting package [50, 51]. A blocking analysis of our raw data shows evidence for autocorrelations up to a blocking length of 10. In our full analysis we use this blocking length, subsequently treating the blocked data as uncorrelated in Monte Carlo time.

We define $\Pi_{LR}(q^2)$ to begin with as an average of $\Pi_{LR}(q_\mu)$ over all lattice momenta q_μ with given length. We find extremely strong correlations between $\Pi_{LR}(q^2)$ values obtained at nearby values of q^2 . In order to estimate the data covariance matrix reliably, we reduce the number of Π_{LR} data points included in the fit. General arguments show that reliable estimation of an $N \times N$ covariance matrix requires $\mathcal{O}(N^2)$ independent measurements [52]. After blocking to remove autocorrelations, our ensembles consist of 60 (Ensemble 1) and 40 (Ensemble 2) independent configurations, allowing for estimation of covariance matrices of dimension $\sqrt{60}$ and $\sqrt{40}$, respectively. We therefore limit the number of points in our fits to 6 or 8.⁹ Due to the strong correlations in the data, this thinning procedure results in minimal loss of statistical information.

In order to thin the data, we choose a ray in momentum space (see Table VI and Fig. 4) and use it to select the values of q^2 . A ray is defined as an integer multiple $q_\mu = na_\mu$ of a generator vector a_μ , which in turn has one or more nonzero components with the minimal value $2\pi/L_\mu$. Each momentum vector q_μ yields a measurement $\Pi_{LR}(q^2)$ which is an average of $\Pi_{LR}(q_\mu^R)$ over lattice rotations and reflections denoted by R ; the transformations $\{R\}$ form the subgroup that does *not* mix time and space axes. $q_\mu = 0$ is always excluded.

Since our lattices have dimension $12^3 \times 24$, any ray $q_\mu = na_\mu$ that has a spatial component can reach at most $n = 6$ without leaving the first Brillouin zone centered on $q = 0$. Thus we

⁹ The fit function (5.1) has 5 parameters, so 6 points still leave us with one degree of freedom.

have automatically six values of $\Pi_{LR}(q^2)$ to fit once the ray is chosen. If a_μ is chosen along the time axis then larger values of n are possible, and here we allow n to reach either 6 or 8 to see whether the results are sensitive to this choice. Each ray with its maximal n defines a maximum momentum q_{\max}^2 , listed in Table VI. Varying the ray furnishes an estimate of the systematic error associated with this thinning of the data.

Another source of systematics lies in choosing the definition of the lattice momentum. In effect, this means choosing between $x = q^2$ and $x = \hat{q}^2$ (see Sec. II C) in defining the fit function (5.1). Sec. V D below summarizes the variation in our results for C_{LR} across these choices.

We take the time-axis fit with a q^2 cutoff at 6 points as our central fit for each ensemble. We show the effect of variations on this scheme below. Even with these thinning schemes, our fits to Eq. (5.1) fail for $m_v > 0.035$. We thus report fit results only for $m_v \leq 0.035$, for each ensemble. We are interested after all in the chiral limit $m_v \rightarrow 0$.

Ray name	Generator a_μ^a	$q_{\max}^2 \equiv \sum_\mu (6a_\mu)^2$
time axis	(0, 0, 0; 1)	2.47
1 spatial axis	(1, 0, 0; 0)	9.87
2 spatial axes	(1, 1, 0; 0)	19.8
3 spatial axes	(1, 1, 1; 0)	29.6
2 mixed axes	(1, 0, 0; 1)	12.3
3 mixed axes	(1, 1, 0; 1)	22.2
4 mixed axes	(1, 1, 1; 1)	32.1

^aMultiply each component by $(2\pi/L_\mu)$.

TABLE VI: Summary of different rays used for thinning in momentum space. We differentiate between spatial and temporal axes because of the $12^3 \times 24$ geometry. See Fig. 4.

C. Testing the validity of the MHA

On the qualitative level, the MHA is a successful formula. All our fits to Eq. (1.7) [via Eq. (5.1)] describe the data well up to $m_v = 0.035$, with $\chi^2/\text{d.o.f.} \lesssim 1$ in all cases (see Fig. 5 for the case of the central fit). On the quantitative level, the MHA is less successful. Table VII compares the central-fit results for masses and decay constants to their spectroscopic values. Figure 6 presents the same information for f_π and m_ρ . The MHA fits are found to reproduce f_π beautifully, yielding numbers and uncertainties comparable to direct measurement.¹⁰ The model's other parameters enjoy markedly less success. In particular, our central-fit results for m_ρ and f_ρ are inconsistent with the measured spectrum. The axial-vector mass is poorly constrained by the MHA, so that it generally agrees with spectroscopy within large uncertainties.

A complementary test within the MHA is to ask how well the Weinberg sum rules are satisfied by the fit parameters; we expect them to hold strictly only in the chiral limit.

¹⁰ This lends confidence to our use of the spectroscopic value of f_π in the direct integration method for estimating C_{LR} .

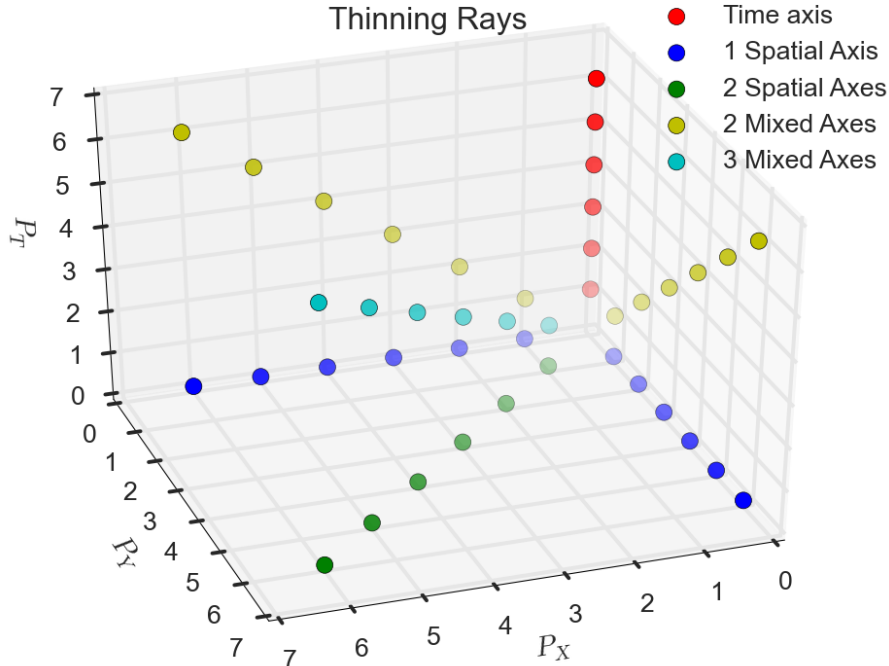


FIG. 4: A schematic view of the rays defined in Table VI for a 3-dimensional lattice.

Figure 7 displays the values of $WSR1 \equiv f_\pi^2 - f_\rho^2 + f_{a_1}^2$ and $WSR2 \equiv f_\rho^2 m_\rho^2 - f_{a_1}^2 m_{a_1}^2$ as functions of valence quark mass; both quantities should be zero in the chiral limit, and this is indeed what we find. What's more, the central fit gives $WSR1$ and $WSR2$ that are consistent with zero (with large error) for all values of m_v up to 0.035.

D. The C_{LR} integral

With the fits to Eq. (5.1) in hand, we proceed to the one-dimensional integral (1.2) for $C_{LR}(m_v)$. We employ trapezoidal integration directly on the lattice data above q_{\max}^2 , and on the sampled fit function below q_{\max}^2 ; carrying out the integral of the fit function analytically yields identical results. To estimate our statistical errors (for given choice of thinning ray and q_{\max}^2), we enclose our analysis inside a bootstrap with 500 resamplings.

To determine C_{LR} in the chiral limit, we must extrapolate from our results at finite fermion mass. As mentioned above, we were able to carry out the MHA fits only for $m_v \leq 0.035$. We again carry out a fully correlated fit, using the bootstrap analysis at each fermion mass m_v with a common set of gauge configuration resamplings to propagate correlations. A quadratic polynomial in m_v is found to describe the data well; we also carry out a cubic polynomial fit as a consistency check. As a further test for systematic effects, we repeat the chiral fits while omitting the lightest mass ($m_v = 0.010$) and omitting the heaviest mass

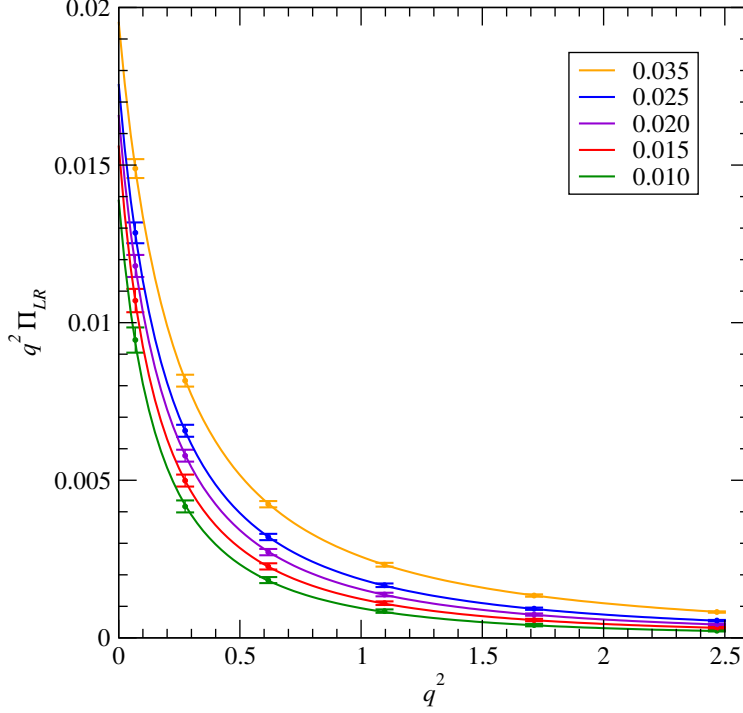


FIG. 5: Fits to $q^2 \Pi_{LR}(q^2)$ with q^μ oriented in the temporal direction (“time axis” ray), on Ensemble 1 data at several values of the valence fermion mass m_v . The data and the fit curves are ordered from heaviest to lightest mass, starting at the top of the figure.

Ensemble 1								
m_v	f_π	MHA	m_ρ	MHA	f_ρ	MHA	m_{a_1}	MHA
0.035	0.140(1)	0.140(2)	0.608(10)	0.526(20)	0.319(13)	0.160(10)	0.886(10)	0.97(14)
0.025	0.135(2)	0.133(2)	0.617(11)	0.480(22)	0.360(15)	0.148(7)	0.879(15)	1.03(20)
0.020	0.128(2)	0.129(2)	0.621(9)	0.456(21)	0.348(3)	0.143(5)	0.846(13)	1.09(16)
0.015	0.127(2)	0.125(3)	0.629(33)	0.425(34)	0.351(5)	0.136(8)	0.853(18)	1.18(46)
0.010	0.120(2)	0.118(3)	0.617(12)	0.420(23)	0.347(4)	0.129(5)	0.818(16)	1.15(22)
Ensemble 2								
m_v	f_π	MHA	m_ρ	MHA	f_ρ	MHA	m_{a_1}	MHA
0.035	0.128(1)	0.126(2)	0.620(9)	0.560(67)	0.336(3)	0.147(24)	0.775(16)	0.82(13)
0.025	0.120(2)	0.114(2)	0.615(12)	0.529(70)	0.344(4)	0.130(38)	0.790(16)	0.79(15)
0.020	0.112(2)	0.106(2)	0.613(11)	0.521(59)	0.340(4)	0.119(35)	0.734(23)	0.71(18)
0.015	0.107(2)	0.099(2)	0.601(18)	0.477(80)	0.341(5)	0.111(33)	0.764(20)	0.79(20)
0.010	0.100(3)	0.090(3)	0.600(17)	0.449(80)	0.339(4)	0.098(29)	0.678(35)	0.73(33)

TABLE VII: Comparison of MHA best-fit parameters to spectroscopy. The MHA value of f_π fits well with spectroscopy, while the ρ -meson parameters disagree. The axial vector mass is generally consistent within large uncertainties.

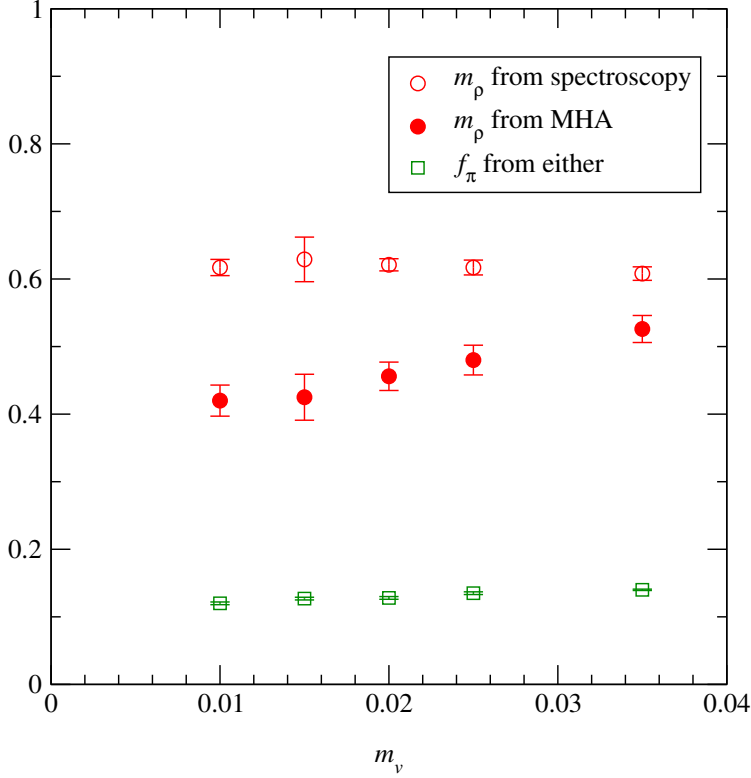


FIG. 6: The pion decay constant f_π and vector meson mass m_ρ from spectroscopy and from the fits of $q^2\Pi_{LR}(q^2)$ to the MHA formula, vs. valence quark mass m_v . The two determinations of f_π are indistinguishable.

($m_v = 0.035$).

Figure 8 shows the results of the chiral extrapolations with the quadratic fits. For comparison, this figure also shows the extrapolated values of C_{LR} from the direct 4d integration described in Sec. IV. The two methods give results that agree within 1σ .

Figure 9 illustrates the stability of our results for C_{LR} in the chiral limit across the many systematic variations discussed above. All in all, we considered the following options:

1. various thinning rays (Table VI) and a quadratic extrapolation,
2. various thinning rays and a cubic extrapolation,
3. time-axis thinning with a q^2 cutoff at 6 or 8 points using a quadratic extrapolation,
4. time-axis thinning with a q^2 cutoff at 6 or 8 points using a cubic extrapolation,
5. time-axis thinning with fixed q^2 cutoff and a quadratic extrapolation, omitting the heaviest or lightest mass, and
6. all of the above, but using \hat{q}^2 instead of q^2 in the fit.

Overall, our results are found to be quite stable, with no significant systematic effects observed. Most importantly, the results present statistically consistent values for C_{LR} which agree with our original 4d direct integration.

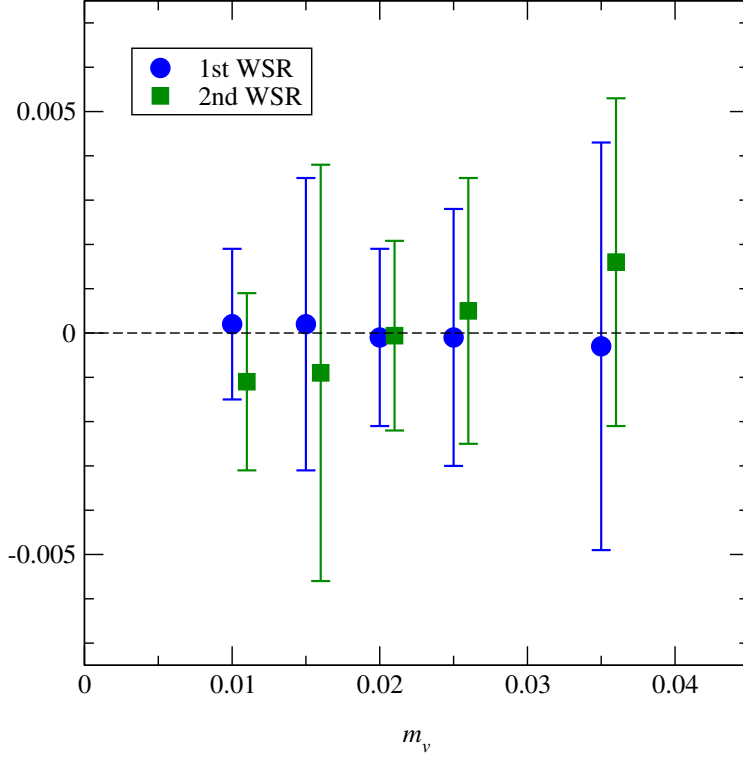


FIG. 7: Test of the first and second Weinberg sum rules, based on the quantities $\text{WSR1} = f_\pi^2 - f_\rho^2 + f_{a_1}^2$ (blue circles) and $\text{WSR2} = f_\rho^2 m_\rho^2 - f_{a_1}^2 m_{a_1}^2$ (green squares). Both quantities are expected to vanish in the limit $m_v \rightarrow 0$.

We believe that the physical reason underlying the stability of our results across the different analysis methods is the rapid falloff of Π_{LR} with momentum. As an illustration, we show in Fig. 10 the fit results for $q^2 \Pi_{LR}(q^2)$ along the 2-spatial-axes ray (see Table VI), for $m_v = 0.035$. This ray reaches a much larger q^2 than the time-axis ray used in Fig. 5. One can see that the value drops by more than three orders of magnitude as q^2 grows towards q_{max}^2 .

As noted in Sec. IV A [Eq. (4.2)], the leading term in the OPE of Π_{LR} is $\sim m_v^2/q^2$, up to logarithms. The large- x behavior of the MHA fit (5.1) allows us to estimate this quantity as b/q^2 . Defining $c = b/m_v^2$, the fit shown in Fig. 10 gives $c = 0.029(3)$. Up to a geometrical factor coming from the shape of the Brillouin zone, c is also the coefficient of the quadratic divergence $m^2 M^2$ discussed in Sec. IV A. Using the above estimate for c we find that the anticipated variation with the cutoff M is indeed of roughly the same size as our statistical uncertainties for the entire range of m_v we have explored. This explains the insensitivity of C_{LR} to the ultraviolet cutoff M that we noted in Sec. IV A.

Our final results for C_{LR} from the MHA fitting method are thus

$$C_{LR} = \begin{cases} 0.00270(24) & \text{Ensemble 1} \\ 0.00115(25) & \text{Ensemble 2} \end{cases} \quad (5.5)$$

The errors quoted here are the statistical errors on the central fit. These results are in good agreement with the direct integration results reported in Table V, although not with each

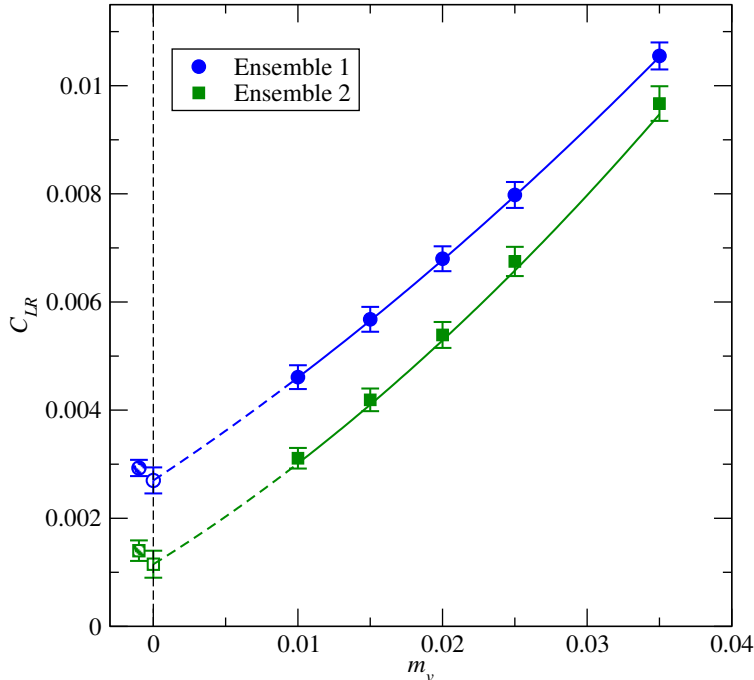


FIG. 8: $C_{LR}(m_v)$ determined with the MHA fits for both ensembles (solid points), and the chiral extrapolations with quadratic polynomials (open points at $m_v = 0$). The extrapolated results show good agreement with those obtained from direct 4d integration (hashed points, displaced horizontally; see Fig. 2.)

other; we refer back to the discussion of Sec. IV C where rescaling by f_π and comparison to QCD are considered.

VI. CONCLUSIONS

We have carried out a pilot study for the calculation of a radiative contribution to the composite Higgs potential using lattice gauge theory. We obtained numerical results for an SU(4) gauge theory with two Dirac fermions in the sextet representation. The electroweak gauge contribution to the potential is determined by the low-energy constant C_{LR} , which can be formulated as an integral over the vacuum polarization function $\Pi_{LR}(q^2)$, calculated straightforwardly on the lattice.

We have demonstrated two approaches to the calculation of the integral: a “direct integration” technique, which sums over $\Pi_{LR}(q^\mu)$ in 4d momentum space, using the value of f_π from spectroscopy to account for the pole at $q^2 = 0$; and a “rational fit” technique, which uses a functional form motivated by the minimal hadron approximation to fit $\Pi_{LR}(q^2)$ at low q^2 . The $q^2 \rightarrow 0$ behavior of the MHA fit gives an alternative determination of f_π which is in good agreement with the spectroscopic value and has similar precision. The direct integration and the rational fit yield consistent results for C_{LR} .

We have investigated the systematics induced by a number of variations in method, particularly in the context of the MHA fit, including thinning of the data along particular rays in q^μ space and variations in the chiral extrapolation. As discussed, these variations

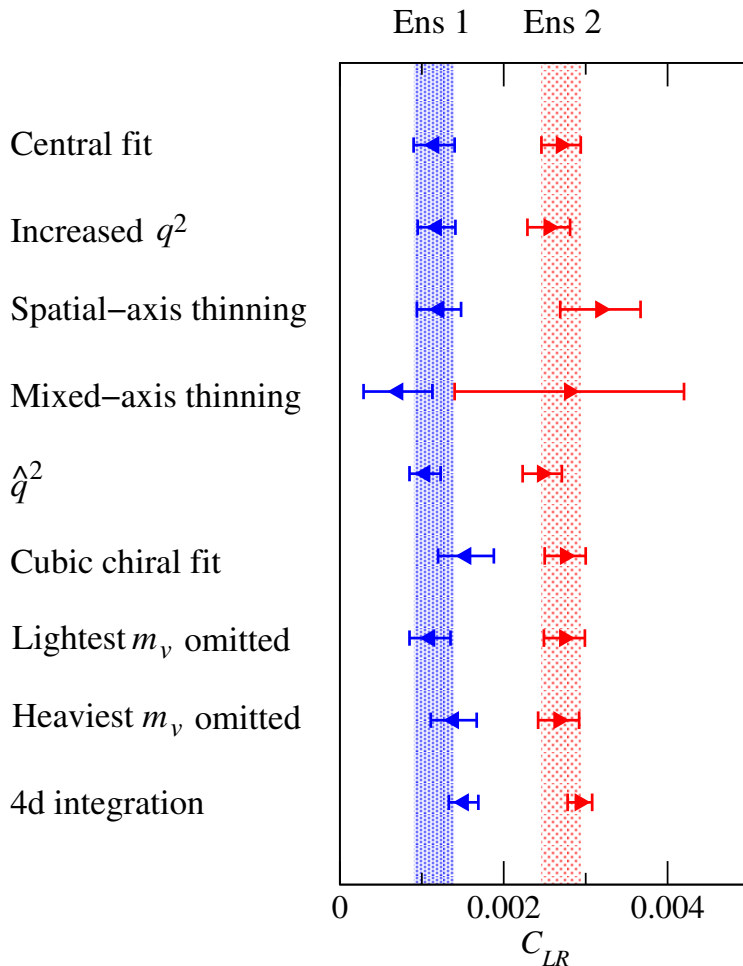


FIG. 9: Error stability plot for $C_{LR}(m_v = 0)$ obtained from ensemble 1 (left) and ensemble 2 (right), comparing the central result to other systematic variations as described in the text. From top to bottom, the variations considered are: increased q_{\max}^2 to fit to 8 points rather than 6; thinning along a spatial axis; thinning along two mixed axes; using \hat{q}^2 instead of q^2 to define the lattice momentum; including a cubic term in the chiral extrapolation; and omitting the lightest and heaviest mass points from the chiral extrapolation. The bottom point is the result of direct integration from Sec. IV. All variations are in agreement with the central fit at roughly 1σ .

show differences of order 1σ or smaller with the central fit. Other sources of systematic error, however, have not been studied in this work. No continuum extrapolation is attempted; neither is the chiral limit of the sea fermions. Moreover, we are not able to estimate possible finite-volume corrections to our results, even though the squeezing of the valence spectra shows that they must be present. Within these limitations, we obtain for the rescaled quantity $r_1^2 C_{LR}/f_\pi^2 \sim 2.3$, consistent between the two ensembles and with the value of C_{LR} in QCD inferred from the $m_{\pi^+} - m_{\pi^0}$ mass difference.

The next step in our program is a calculation of C_{LR} in an $SU(4)$ gauge theory with both fundamental and sextet fermions, for application to the composite Higgs model of Refs. [8, 11]. Simulation with two Dirac fermions in each representation would be a deviation from the full model, which requires 5 species of Majorana fermions in the sextet representation and 3

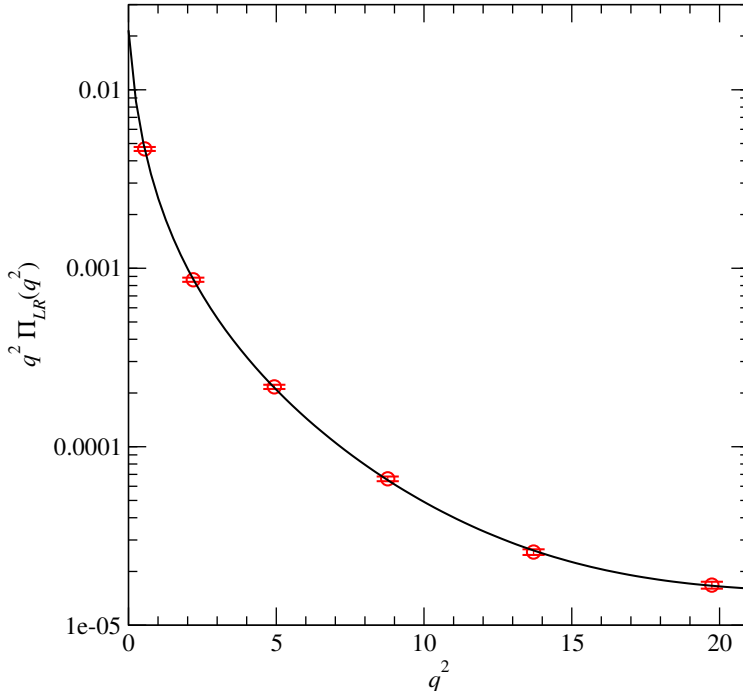


FIG. 10: Logarithmic plot of $q^2 \Pi_{LR}(q^2)$ with q^μ oriented along the “2-spatial-axes” ray, on Ensemble 1 data with valence fermion mass $m_v = 0.035$.

Dirac fermions in the fundamental; nonetheless, it should furnish a reasonable approximation while allowing use of the standard hybrid Monte Carlo method. Calculation of the phase diagram and spectrum of this theory is now underway [53].

Acknowledgments

This material is based upon work supported by the U.S. Department of Energy, Office of Science, Office of High Energy Physics, under Award Number DE-SC0010005 (T. D. and E. N.) and Number DE-FG03-92ER40711 (M. G.). This work was also supported in part by the Israel Science Foundation under grant no. 449/13. Brookhaven National Laboratory is supported by the U. S. Department of Energy under contract DE-SC0012704.

Y. S. thanks San Francisco State University, and M. G., Y. S., and B. S. thank the University of Colorado, for hospitality. B. S. also thanks Prof. Ting-Wai Chiu for arranging the hospitality of National Taiwan University, where his visit was supported by Taiwan Ministry of Science and Technology under grant no. MOST 103-2811-M-002-040. Part of this paper was written while B. S. and E. N. were at the Kavli Institute for Theoretical Physics in Santa Barbara, CA; the KITP is supported in part by the National Science Foundation under grant no. NSF PHY11-25915.

Computations were performed on clusters of the University of Colorado theory group and of the Tel Aviv University lattice group. Our computer code is based on version 7 of the publicly available code of the MILC collaboration [54].

Appendix A: The NDS term in the action

We describe briefly the NDS term [32] and the reason for its inclusion in the action.

nHYP smearing [29] is a three-step process. In the first step, we average a link $U_{x\rho}$ with two staples in one of the planes containing the link, giving

$$\Omega = (1 - \alpha_3)U_{x\rho} + \frac{\alpha_3}{2} \left(U_{x\xi}U_{x+\hat{\xi},\rho}U_{x+\hat{\rho},\xi}^\dagger + U_{x-\hat{\xi},\xi}^\dagger U_{x-\hat{\xi},\rho}U_{x-\hat{\xi}+\hat{\rho},\xi} \right). \quad (\text{A1})$$

We then project Ω back to $U(4)$ via

$$\bar{V}_{x,\rho;\xi} = \Omega \bar{Q}^{-1/2}, \quad (\text{A2})$$

where

$$\bar{Q} = \Omega^\dagger \Omega. \quad (\text{A3})$$

The following two steps in the smearing average \bar{V} in the other two planes successively, projecting again each time; we write schematically $U \rightarrow \bar{V} \rightarrow \tilde{V} \rightarrow V$, whereupon the fermion action is constructed from the final V links.

Let us focus on the first step. Since the fermion action contains smeared links V , the molecular-dynamics force on the thin link $U_{x\rho}$ is calculated through a chain rule [30] that contains derivatives $\partial\bar{V}/\partial U$. If one of the plaquettes containing the staples in Eq. (A1) contains a large field strength (i.e., a dislocation) then Ω may be far from unitary, and \bar{Q} may possess a small eigenvalue. Then the derivative of Eq. (A2) can be very large. Using this force in the time step will introduce a large error in the integration and lead inevitably to rejection of the trajectory. Since the dislocation is a property of the initial gauge field, it can be very hard for the system to find its way to an acceptable trajectory.

The NDS prescription is designed to keep the system away from regions of phase space where \bar{Q} has small eigenvalues. Naturally, it does this for all three steps of the smearing. The new term in the action takes the simple form,

$$S_{\text{NDS}} = \frac{1}{2N_c} \sum_x \text{tr} \left(\gamma_1 \sum_\mu Q_{x,\mu}^{-1} + \gamma_2 \sum_{\mu \neq \nu} \tilde{Q}_{x,\mu;\nu}^{-1} + \gamma_3 \sum_{\rho \neq \xi} \bar{Q}_{x,\rho;\xi}^{-1} \right), \quad (\text{A4})$$

where \tilde{Q} and Q are the counterparts of \bar{Q} for the two later smearing steps. In practice, we take $\gamma_1 = \gamma_2 = \gamma_3 \equiv \gamma$. This is a pure-gauge term; in weak coupling it shifts the bare coupling according to Eq. (2.2).

Appendix B: The pole at $q^2 = 0$

We rederive here the pion pole contribution to the axial-current two-point function. Consider first the massless case. From the definition of the pion decay constant one might write

$$\langle A_\mu A_\nu \rangle (q) = -f_\pi^2 \frac{q_\mu q_\nu}{q^2} \quad (\text{incomplete}). \quad (\text{B1})$$

Here A_μ is the axial current, $\langle A_\mu A_\nu \rangle (q)$ is the four-dimensional Fourier transform, and we have neglected the contribution of all other resonances. It was noted long ago by Brout and

Englert [55] that current conservation requires the presence of a contact term in order that the right-hand side of Eq. (B1) be transverse. With the contact term added, the result is

$$\langle A_\mu A_\nu \rangle(q) = f_\pi^2 (\delta_{\mu\nu} - q_\mu q_\nu / q^2) = f_\pi^2 P_{\mu\nu}^\perp . \quad (\text{B2})$$

Proceeding to the case of a massive pion, we find that the contact term remains unchanged, while the location of the pole moves:

$$\begin{aligned} \langle A_\mu A_\nu \rangle(q) &= f_\pi^2 \left(\delta_{\mu\nu} - \frac{q_\mu q_\nu}{q^2 + m_\pi^2} \right) \\ &= f_\pi^2 \left(\delta_{\mu\nu} - \frac{q_\mu q_\nu}{q^2} \right) \\ &\quad + f_\pi^2 q_\mu q_\nu \left(\frac{1}{q^2} - \frac{1}{q^2 + m_\pi^2} \right) \\ &= P_{\mu\nu}^\perp f_\pi^2 + P_{\mu\nu}^\parallel \frac{f_\pi^2 m_\pi^2}{q^2 + m_\pi^2} , \end{aligned} \quad (\text{B3})$$

where $P_{\mu\nu}^\parallel = q_\mu q_\nu / q^2$. The coefficient of the transverse projector P^\perp is always f_π^2 , irrespective of m_π —the dependence on the pion mass is entirely in the longitudinal part. This result can be traced back to the derivative coupling of the pion field to the axial current. It follows that the pion's contribution to $\Pi_{LR}(q^2)$ is f_π^2/q^2 , for both massless and massive pions. The decay constant f_π depends, of course, on the quark mass, as does the asymptotic large- q^2 behavior.

Appendix C: Mixed action chiral perturbation theory for the valence decay constant

We saw in Sec. IVC that there is good agreement between the values of $r_1^2 C_{LR}(m_v)/f_\pi^2(m_v)$ for the two ensembles when we extrapolate to the valence chiral limit $m_v \rightarrow 0$. In this appendix we attempt to take this one step further. We study the measured valence decay constants using mixed-action chiral perturbation theory (χ PT), to see if we can obtain a prediction for the continuum limit of the decay constant. Combined with Eq. (4.17), this would allow us to make a prediction for the continuum limit of C_{LR} itself. As it turns out, we cannot obtain a reliable limit for the decay constant from our data. We discuss the possible reasons for this state of affairs.

1. f_{vv} as a function of m_v

Following the conventions of χ PT, in this appendix we refer to the valence pion mass and decay constant as $M_{vv}(m_v)$ and $f_{vv}(m_v)$, respectively. Since r_1 is practically the same for both ensembles, instead of working with the dimensionless quantity $r_1 f_{vv}$ we might as well use directly the results reported in lattice units in Tables III and IV.

In $N_f = 2$ QCD with Wilson sea quarks and chiral valence quarks, the valence decay

constant f_{vv} is given at the next-to-leading order (NLO) by [56–63]¹¹

$$\begin{aligned} \frac{f_{vv,NLO}}{f} &= 1 - \frac{M_{0,vs}^2}{8\pi^2 f^2} \log\left(\frac{M_{0,vs}^2}{\mu^2}\right) \\ &+ \frac{8}{f^2}(L_5 M_{0,vv}^2 + 2L_4 M_{0,ss}^2) + \hat{a}^2 \mathcal{D} . \end{aligned} \quad (C1)$$

The leading-order (LO) pion masses are

$$M_{0,vv}^2 = 2Bm_v , \quad (C2)$$

$$M_{0,ss}^2 = 2(BZm_s + \hat{a}^2 \mathcal{D}_{ss}) , \quad (C3)$$

$$M_{0,vs}^2 = \frac{1}{2}(M_{0,vv}^2 + M_{0,ss}^2) + \hat{a}^2 \mathcal{D}_{vs} . \quad (C4)$$

Here f and B are the usual parameters of the LO continuum chiral lagrangian, f being the decay constant in the chiral limit. L_4 and L_5 are NLO parameters of continuum χ PT [56]. The parameters \mathcal{D} , \mathcal{D}_{ss} and \mathcal{D}_{vs} are linear combinations of the LO low-energy constants of mixed-action χ PT. \hat{a} is a rescaled version of the lattice spacing a , roughly, $\hat{a} \sim \Lambda^3 a$, where Λ is the confinement scale [59, 60]. The extra Z factor in Eq. (C3) arises because our sea-quark’s axial current is not properly normalized, and this renormalization factor has to be removed from the measured Wilson sea quark’s mass. In other words, the correct sea-quark mass is Zm_s .

In principle we need to adapt Eq. (C1) to $N_f = 2$ Dirac fermions in a real representation, for which the coset structure is $SU(2N_f)/SO(2N_f)$ rather than the familiar $[SU(N_f)_L \times SU(N_f)_R]/SU(N_f)$ for QCD. It turns out that the coefficient of the logarithm is unchanged. Also, while NLO mixed-action results for a real representation are not available, one can argue that the $O(a^2)$ terms present in Eqs. (C1), (C3), and (C4) are the most general possible, and thus, this part of Eq. (C1) is fine, too.

We will be comparing ensembles with different lattice actions, as well as different sea masses. We lump these differences together by rewriting Eq. (C4) as

$$M_{0,vs}^2 = Bm_v + A , \quad (C5)$$

where

$$A = \frac{1}{2}M_{0,ss}^2 + \hat{a}^2 \mathcal{D}_{vs} = BZm_s + \hat{a}^2(\mathcal{D}_{ss} + \mathcal{D}_{vs}) . \quad (C6)$$

Similarly,

$$C = 32L_4(BZm_s + \hat{a}^2 \mathcal{D}_{ss})/f^2 + \hat{a}^2 \mathcal{D} , \quad (C7)$$

$$D = 16L_5 B/f^2 . \quad (C8)$$

Taking the renormalization scale to be $\mu = \sqrt{8}\pi f$, Eq. (C1) takes the form¹²

$$f_{vv,NLO} = f \left[1 - \left(\frac{A + Bm_v}{8\pi^2 f^2} \right) \log\left(\frac{A + Bm_v}{8\pi^2 f^2} \right) + C + Dm_v \right] , \quad (C9)$$

¹¹ Most of the χ PT literature uses the convention $\langle 0 | A_\mu^a(x) | \pi^b(p) \rangle = i\sqrt{2} p_\mu f_\pi \delta^{ab} e^{ipx}$. In order to adapt to our convention, Eq. (3.2), we make the replacement $f_\pi \rightarrow f_\pi/\sqrt{2}$ in the relevant χ PT formulae.

¹² We assume that $L_{4,5}$ have been defined with the same renormalization scale.

\tilde{B}	\tilde{A}	\tilde{A}'	\tilde{D}	\tilde{C}	\tilde{C}'	$\chi^2/\text{d.o.f.}$
0.358(62)	0.010(6)	-0.001(3)	-0.324(72)	0.065(21)	0.089(15)	3.1/6

TABLE VIII: Fit parameters for Eq. (C11).

In fact, this parametrization suffers from a redundancy. Eq. (C9) is invariant under the reparametrization

$$\begin{aligned}
f &\rightarrow xf, \\
A &\rightarrow xA, \\
B &\rightarrow xB, \\
C &\rightarrow x^{-1}(1-x+C) - (8\pi^2 f^2 x)^{-1} A \log(x), \\
D &\rightarrow x^{-1}D - (8\pi^2 f^2 x)^{-1} B \log(x),
\end{aligned}
\tag{C10}$$

showing that one parameter in Eq. (C9) can be eliminated. Indeed, we can write Eq. (C9) in the form

$$f_{vv,NLO} = -(\tilde{A} + \tilde{B}m_v) \log(\tilde{A} + \tilde{B}m_v) + \tilde{C} + \tilde{D}m_v, \tag{C11}$$

by defining

$$\begin{aligned}
\tilde{A} &= A/(8\pi^2 f), \\
\tilde{B} &= B/(8\pi^2 f), \\
\tilde{C} &= f(1+C) + \tilde{A} \log(f), \\
\tilde{D} &= fD + \tilde{B} \log(f).
\end{aligned}
\tag{C12}$$

The fit parameters \tilde{B} and \tilde{D} depend only on the low-energy constants of continuum χ PT, so they are universal. The parameters \tilde{A} and \tilde{C} depend on the details of the lattice action, as well as on the sea mass, so they are different for the two ensembles. We reserve \tilde{A} and \tilde{C} for Ensemble 1, and denote the corresponding parameter of Ensemble 2 by \tilde{A}' and \tilde{C}' . This makes a total of 6 parameters.

The result of the fit is shown in Table VIII. While the quality of the fit is good, the reparametrization freedom prevents us from determining f . Several comments are in order.

First, what we are calculating is $f_{vv,NLO} = f_{vv,NLO}(m_s, m_v, \hat{a})$. The fit (C11) allows us in principle to determine $f_{vv,NLO}(m_s, 0, \hat{a})$ from the valence chiral extrapolation. However, this extrapolation is mathematically inconsistent if \tilde{A} or \tilde{A}' are negative, because the argument of the logarithm becomes ill-defined. We return to this issue below.

Second, additional data at different values of the sea mass m_s and the lattice spacing \hat{a} would in principle allow us to do also the sea-chiral extrapolation and the continuum extrapolation, obtaining $f_{vv,NLO}(0, 0, 0) = f$, the (continuum) decay constant in the chiral limit. In other words, the fit does know about f in spite of the reparametrization freedom, but only through its dependence on all three parameters— m_s , m_v , and \hat{a} .

Third, if we include finite-volume corrections in the χ PT formulae, the reparametrization freedom disappears. In principle, this allows us to determine f . In practice, however, the finite-volume NLO correction to f_{vv} is small, and as a result, f is poorly determined. This correction is small because the pion that runs in the loop is a mixed pion [see Eq. (C1)]. As a result, the finite-volume correction is not sensitive to the valence pion's mass M_{vv} , but only to the mixed pion's mass M_{vs} , which is significantly larger.

data set	f	\hat{A}	\hat{A}'	\hat{D}	\hat{C}	\hat{C}'	\hat{E}	$\chi^2/\text{d.o.f.}$
1	0.07(2)	0.03(7)	-0.07(3)	2.2(16)	0.5(5)	0.4(3)	–	0.16/2
2	0.07(2)	0.03(6)	-0.07(3)	2.0(12)	0.4(3)	0.3(2)	–	0.16/2
2	0.0346(7)	0.13(7)	-0.13(5)	8.3(6)	1.8(1)	1.3(1)	6.5(12)	0.014/1

TABLE IX: Fit parameters for Eq. (C13). Each fit uses 4 values of m_v . For set 1 we used data from Ensembles 1 and 2 for the masses 0.02, 0.035, 0.05 and 0.075; for set 2, 0.075 was replaced by 0.1. The first two lines are 6-parameter fits. The last line uses set 2 again, but has an added NNLO analytic term $\hat{E}M_{vv}^4$, for a total of 7 parameters.

Finally, we note that the reparametrization freedom is quite generic in Wilson χ PT. For example, it is also found in the NLO formula for the dependence of $M_{vv,NLO}^2$ on m_v .

2. f_{vv} as a function of M_{vv}

As an alternative strategy we may fit f_{vv} as a function of the valence pseudoscalar mass. Thanks to the absence of B at the order we are working, there is no reparametrization freedom, and it is possible to determine f . The fit form is obtained by replacing $2Bm_v$ by $M_{0,vv}^2$ in Eq. (C9), and then replacing $M_{0,vv}^2$ by the actual measured mass of the valence pion, M_{vv} . Explicitly,

$$f_{vv,NLO} = f \left[1 - (\hat{A} + \hat{M}_{vv}^2) \log(\hat{A} + \hat{M}_{vv}^2) + \hat{C} + \hat{D}M_{vv}^2 \right], \quad (\text{C13})$$

where

$$\begin{aligned} \hat{M}_{vv}^2 &= M_{vv}^2 / (16\pi^2 f^2), \\ \hat{A} &= A / (8\pi^2 f^2), \\ \hat{C} &= C, \\ \hat{D} &= D / (2B). \end{aligned} \quad (\text{C14})$$

Since we are now fitting data with errors as a function of data with errors, the χ^2 function takes the form¹³

$$\chi^2 = \sum_{i=1}^n \left[\frac{(f_i - f(x_i; \alpha_p))^2}{\delta f_i^2} + \frac{(m_i - x_i)^2}{\delta m_i^2} \right]. \quad (\text{C15})$$

Here $(f_i, \delta f_i)$ are the measured values and errors of the valence decay constant, while $(m_i, \delta m_i)$ are the corresponding data for the valence pion mass (see Tables III and IV). The fit parameters include $\alpha_p = \{f, \hat{A}, \hat{A}', \hat{D}, \hat{C}, \hat{C}'\}$, as well as the x_i , which are the true values of the valence pion's mass. Notice that the number of degrees of freedom in Eq. (C15) is the same as for the fit (C9).

¹³ For simplicity we display the χ^2 function for uncorrelated data. In the actual fit we have taken the cross-correlations into account.

Fit results are displayed in Table IX. In all cases the fit’s predictions for the true valence pion’s mass, x_i , are consistent with the data, and so we do not display them. While the fit quality is very good, the errors are rather large. However, there is a more serious problem.

Mixed-action QCD satisfies the mass inequality [64]¹⁴

$$M_{vs} \geq \min(M_{ss}, M_{vv}) . \quad (\text{C16})$$

Inequality (C16) must be respected at each order in mixed-action χ PT, and for any choice of the quark masses (as long as the masses are not so large that χ PT breaks down). Constraints on the low-energy constants can be derived by examining particular limits of the quark masses. First, we tune the quark masses such that the sea and valence pions have equal tree-level masses, $M_{0,ss} = M_{0,vv}$. Using Eq. (C4) it follows that we must have

$$\mathcal{D}_{vs} \geq 0 . \quad (\text{C17})$$

A second inequality follows by considering the double chiral limit, $(m_s, m_v) \rightarrow 0$. Then $M_{0,vs} \rightarrow \hat{a}^2(\mathcal{D}_{ss} + \mathcal{D}_{vs})$, and, in order that $M_{0,vs}^2$ not become negative [in clear violation of Eq. (C16)], we must have

$$\mathcal{D}_{ss} + \mathcal{D}_{vs} \geq 0 . \quad (\text{C18})$$

What is important for us is that, using Eq. (C6), the inequality (C17) translates into

$$A \geq M_{0,ss}^2/2 , \quad (\text{C19})$$

or, equivalently,

$$\hat{A} \geq M_{0,ss}^2/(16\pi^2 f^2) . \quad (\text{C20})$$

Using the result for f from Table IX (without the \hat{E} term in the fit), the ball-park values of this bound are about 0.4 for Ensemble 1 (i.e., \hat{A}), and 0.2 for Ensemble 2 (i.e., \hat{A}'). The fit results for \hat{A} and \hat{A}' are in bad disagreement with these bounds.

At a technical level, these difficulties have to do with the large curvature in the plots of the data for $f_{vv}(M_{vv}^2)$. Ensemble 2 has the larger curvature, and, mathematically, the fit makes up for it by demanding a negative \hat{A}' . The bound (C20) is far from satisfied. Moreover, as the argument of the logarithm is $\hat{A} + \hat{M}_{vv}^2/2$, the chiral valence extrapolation is mathematically impossible. In order to avoid this large curvature we would have to work at smaller (valence and sea) masses, which, in turn, would require larger lattices to accommodate the pions.

-
- [1] H. Georgi and D. B. Kaplan, “Composite Higgs and Custodial SU(2),” *Phys. Lett. B* **145**, 216 (1984).
 - [2] M. J. Dugan, H. Georgi and D. B. Kaplan, “Anatomy of a Composite Higgs Model,” *Nucl. Phys. B* **254**, 299 (1985).
 - [3] R. Contino, “The Higgs as a Composite Nambu–Goldstone Boson,” arXiv:1005.4269 [hep-ph].
 - [4] B. Bellazzini, C. Csáki and J. Serra, “Composite Higgses,” *Eur. Phys. J. C* **74**, 2766 (2014) [arXiv:1401.2457 [hep-ph]].

¹⁴ See also Ref. [65].

- [5] G. Panico and A. Wulzer, “The Composite Nambu-Goldstone Higgs,” *Lect. Notes Phys.* **913**, 1 (2016) [arXiv:1506.01961 [hep-ph]].
- [6] M. E. Peskin, “The Alignment of the Vacuum in Theories of Technicolor,” *Nucl. Phys. B* **175**, 197 (1980).
- [7] J. Barnard, T. Gherghetta and T. S. Ray, “UV descriptions of composite Higgs models without elementary scalars,” *JHEP* **1402**, 002 (2014) [arXiv:1311.6562 [hep-ph]].
- [8] G. Ferretti, “UV Completions of Partial Compositeness: The Case for an SU(4) Gauge Group,” *JHEP* **1406**, 142 (2014) [arXiv:1404.7137 [hep-ph]].
- [9] L. Vecchi, “A ‘dangerous irrelevant’ UV-completion of the composite Higgs,” arXiv:1506.00623 [hep-ph].
- [10] T. Ma and G. Cacciapaglia, “Fundamental Composite 2HDM: SU(N) with 4 flavours,” *JHEP* **1603**, 211 (2016) [arXiv:1508.07014 [hep-ph]].
- [11] G. Ferretti, “Gauge theories of Partial Compositeness: Scenarios for Run-II of the LHC,” arXiv:1604.06467 [hep-ph].
- [12] G. Ferretti and D. Karateev, “Fermionic UV completions of Composite Higgs models,” *JHEP* **1403**, 077 (2014) [arXiv:1312.5330 [hep-ph]].
- [13] D. B. Kaplan, “Flavor at SSC energies: A New mechanism for dynamically generated fermion masses,” *Nucl. Phys. B* **365**, 259 (1991).
- [14] T. DeGrand, “Lattice tests of beyond Standard Model dynamics,” *Rev. Mod. Phys.* **88**, 015001 (2016) [arXiv:1510.05018 [hep-ph]].
- [15] M. Golterman and Y. Shamir, “Top quark induced effective potential in a composite Higgs model,” *Phys. Rev. D* **91**, 094506 (2015) [arXiv:1502.00390 [hep-ph]].
- [16] M. Golterman and Y. Shamir, “Vacuum alignment and lattice artifacts: Wilson fermions,” *Phys. Rev. D* **89**, 054501 (2014) [arXiv:1401.0356 [hep-lat]].
- [17] E. Witten, “Some Inequalities Among Hadron Masses,” *Phys. Rev. Lett.* **51**, 2351 (1983).
- [18] T. Das, G. S. Guralnik, V. S. Mathur, F. E. Low and J. E. Young, “Electromagnetic mass difference of pions,” *Phys. Rev. Lett.* **18**, 759 (1967).
- [19] E. Shintani *et al.* [JLQCD Collaboration], “ S -parameter and pseudo-Nambu-Goldstone boson mass from lattice QCD,” *Phys. Rev. Lett.* **101**, 242001 (2008) [arXiv:0806.4222 [hep-lat]].
- [20] E. Shintani *et al.* [JLQCD Collaboration and TWQCD Collaboration], “Lattice study of the vacuum polarization function and determination of the strong coupling constant,” *Phys. Rev. D* **79**, 074510 (2009) [arXiv:0807.0556 [hep-lat]].
- [21] R. Gupta, G. Kilcup and S. R. Sharpe, “One Loop Lattice Vacuum Energy,” *Phys. Lett. B* **147**, 339 (1984).
- [22] T. DeGrand, Y. Liu, E. T. Neil, Y. Shamir and B. Svetitsky, “Spectroscopy of SU(4) gauge theory with two flavors of sextet fermions,” *Phys. Rev. D* **91**, 114502 (2015) [arXiv:1501.05665 [hep-lat]].
- [23] H. Neuberger, “Exactly massless quarks on the lattice,” *Phys. Lett. B* **417**, 141 (1998) [arXiv:hep-lat/9707022].
- [24] H. Neuberger, “A practical implementation of the overlap-Dirac operator,” *Phys. Rev. Lett.* **81**, 4060 (1998) [arXiv:hep-lat/9806025].
- [25] P. A. Boyle, L. Del Debbio, J. Wennekers and J. M. Zanotti [RBC and UKQCD collaborations], “The S Parameter in QCD from Domain Wall Fermions,” arXiv:0909.4931 [hep-lat].
- [26] T. Appelquist *et al.* [LSD Collaboration], “Parity Doubling and the S Parameter Below the Conformal Window,” *Phys. Rev. Lett.* **106**, 231601 (2011) [arXiv:1009.5967 [hep-ph]].
- [27] S. Weinberg, “Precise relations between the spectra of vector and axial vector mesons,” *Phys.*

- Rev. Lett. **18**, 507 (1967).
- [28] B. Sheikholeslami and R. Wohlert, “Improved Continuum Limit Lattice Action For QCD With Wilson Fermions,” Nucl. Phys. B **259**, 572 (1985).
 - [29] A. Hasenfratz and F. Knechtli, “Flavor symmetry and the static potential with hypercubic blocking,” Phys. Rev. D **64**, 034504 (2001) [arXiv:hep-lat/0103029].
 - [30] A. Hasenfratz, R. Hoffmann and S. Schaefer, “Hypercubic smeared links for dynamical fermions,” JHEP **0705**, 029 (2007). [hep-lat/0702028].
 - [31] T. DeGrand, Y. Shamir and B. Svetitsky, “SU(4) lattice gauge theory with decuplet fermions: Schrödinger functional analysis,” Phys. Rev. D **85**, 074506 (2012) [arXiv:1202.2675 [hep-lat]].
 - [32] T. DeGrand, Y. Shamir and B. Svetitsky, “Suppressing dislocations in normalized hypercubic smearing,” Phys. Rev. D **90**, no. 5, 054501 (2014) [arXiv:1407.4201 [hep-lat]].
 - [33] Y. Shamir, B. Svetitsky and E. Yurkovsky, “Improvement via hypercubic smearing in triplet and sextet QCD,” Phys. Rev. D **83**, 097502 (2011) [arXiv:1012.2819 [hep-lat]].
 - [34] T. A. DeGrand [MILC collaboration], “A variant approach to the overlap action,” Phys. Rev. D **63**, 034503 (2000) [arXiv:hep-lat/0007046].
 - [35] T. A. DeGrand and S. Schaefer, “Physics issues in simulations with dynamical overlap fermions,” Phys. Rev. D **71**, 034507 (2005) [arXiv:hep-lat/0412005].
 - [36] T. DeGrand and S. Schaefer, “Simulating an arbitrary number of flavors of dynamical overlap fermions,” JHEP **0607**, 020 (2006) [arXiv:hep-lat/0604015].
 - [37] T. DeGrand and S. Schaefer, “Parameters of the lowest order chiral Lagrangian from fermion eigenvalues,” Phys. Rev. D **76**, 094509 (2007) [arXiv:0708.1731 [hep-lat]].
 - [38] T. DeGrand, Z. Liu and S. Schaefer, “Quark condensate in two-flavor QCD,” Phys. Rev. D **74**, 094504 (2006) [Erratum-ibid. D **74**, 099904 (2006)] [arXiv:hep-lat/0608019].
 - [39] S. Capitani, M. Gockeler, R. Horsley, P. E. Rakow and G. Schierholz, “Operator improvement for Ginsparg–Wilson fermions,” Phys. Lett. B **468**, 150 (1999) [arXiv:hep-lat/9908029].
 - [40] T. A. DeGrand [MILC Collaboration], “Kaon B parameter in quenched QCD,” Phys. Rev. D **69**, 014504 (2004) [hep-lat/0309026].
 - [41] A. Stathopoulos, SIAM J. Sci. Comput. **29**, 481 (2007); A. Stathopoulos and J. R. McCombs, SIAM J. Sci. Comput., **29**, 2162 (2007).
 - [42] C. Aubin, T. Blum, P. Chau, M. Golterman, S. Peris and C. Tu, “Finite-volume effects in the muon anomalous magnetic moment on the lattice,” arXiv:1512.07555 [hep-lat].
 - [43] T. DeGrand, “Oblique correction in a walking lattice theory,” arXiv:1006.3777 [hep-lat].
 - [44] G. P. Lepage and P. B. Mackenzie, “On the viability of lattice perturbation theory,” Phys. Rev. D **48**, 2250 (1993) [hep-lat/9209022].
 - [45] T. Blum *et al.*, “Quenched lattice QCD with domain wall fermions and the chiral limit,” Phys. Rev. D **69**, 074502 (2004) [hep-lat/0007038].
 - [46] K. Cichy, G. Herdoiza and K. Jansen, “Continuum Limit of Overlap Valence Quarks on a Twisted Mass Sea,” Nucl. Phys. B **847**, 179 (2011) [arXiv:1012.4412 [hep-lat]].
 - [47] K. Cichy, V. Drach, E. Garcia-Ramos, G. Herdoiza and K. Jansen, “Overlap valence quarks on a twisted mass sea: a case study for mixed action Lattice QCD,” Nucl. Phys. B **869**, 131 (2013) [arXiv:1211.1605 [hep-lat]].
 - [48] E. Corrigan and P. Ramond, “A Note on the Quark Content of Large Color Groups,” Phys. Lett. B **87**, 73 (1979).
 - [49] C. Aubin, T. Blum, M. Golterman and S. Peris, “Model-independent parametrization of the hadronic vacuum polarization and $g - 2$ for the muon on the lattice,” Phys. Rev. D **86**, 054509 (2012) [arXiv:1205.3695 [hep-lat]].

- [50] G. P. Lepage, “`lsqfit v4.8.5.1`”, [dx.doi.org/10.5281/zenodo.10236](https://doi.org/10.5281/zenodo.10236)
- [51] G. P. Lepage, B. Clark, C. T. H. Davies, K. Hornbostel, P. B. Mackenzie, C. Morningstar and H. Trotter, “Constrained curve fitting,” Nucl. Phys. Proc. Suppl. **106**, 12 (2002) [hep-lat/0110175].
- [52] C. Michael, “Fitting correlated data,” Phys. Rev. D **49**, 2616 (1994) [hep-lat/9310026].
- [53] Work in progress by T. DeGrand, D. Hackett, W. Jay, E. Neil, Y. Shamir, B. Svetitsky, and N. Tamir.
- [54] <http://www.physics.utah.edu/~Edetar/milc/>
- [55] F. Englert and R. Brout, “Broken Symmetry and the Mass of Gauge Vector Mesons,” Phys. Rev. Lett. **13**, 321 (1964).
- [56] J. Gasser and H. Leutwyler, “Chiral Perturbation Theory: Expansions in the Mass of the Strange Quark,” Nucl. Phys. B **250**, 465 (1985).
- [57] J. Bijnens and J. Lu, “Technicolor and other QCD-like theories at next-to-next-to-leading order,” JHEP **0911**, 116 (2009) [arXiv:0910.5424 [hep-ph]].
- [58] M. Golterman, “Applications of chiral perturbation theory to lattice QCD,” arXiv:0912.4042 [hep-lat].
- [59] G. Rupak and N. Shoresh, “Chiral perturbation theory for the Wilson lattice action,” Phys. Rev. D **66**, 054503 (2002) [hep-lat/0201019].
- [60] O. Bär, G. Rupak and N. Shoresh, “Simulations with different lattice Dirac operators for valence and sea quarks,” Phys. Rev. D **67**, 114505 (2003) [hep-lat/0210050].
- [61] O. Bär, G. Rupak and N. Shoresh, “Chiral perturbation theory at $O(a^2)$ for lattice QCD,” Phys. Rev. D **70**, 034508 (2004) [hep-lat/0306021].
- [62] O. Bär, C. Bernard, G. Rupak and N. Shoresh, “Chiral perturbation theory for staggered sea quarks and Ginsparg-Wilson valence quarks,” Phys. Rev. D **72**, 054502 (2005) [hep-lat/0503009].
- [63] O. Bär, “Chiral Perturbation Theory for Lattice QCD,” habilitation thesis, Humboldt University of Berlin (2011), <http://edoc.hu-berlin.de/docviews/abstract.php?id=37831>
- [64] O. Bär, M. Golterman and Y. Shamir, “Flavor symmetry breaking in lattice QCD with a mixed action,” Phys. Rev. D **83**, 054501 (2011) [arXiv:1012.0987 [hep-lat]].
- [65] M. T. Hansen and S. R. Sharpe, “Constraint on the Low Energy Constants of Wilson Chiral Perturbation Theory,” Phys. Rev. D **85**, 014503 (2012) [arXiv:1111.2404 [hep-lat]].